CORRELATION BETWEEN DIFFRACTION AND INELASTIC SCATTERING OF X-RAYS IN CRYSTALS

Yasuji KASHIWASE, Motokazu KOGISO* and Masahiro MORI*

*Department of Applied Physics, *School of Informatics and Sciences,
Department of Natural Science Informatics*

(Received October 18, 1995)

Abstract

X-ray thermal diffuse scattering (TDS) as well as Compton scattering in crystal yields diffraction pattern similar to Kikuchi-pattern in electron diffraction. Fluorescent X-rays yield Kossel-pattern. Intensity of inelastic scattering from a nearly perfect crystal varies when glancing angle of the incident beam varies across the Bragg angle. The above two phenomena are considered to be in relation of reciprocal processes. The diffraction pattern depends upon crystal perfection, wavelength and crystal thickness. A review on these theoretical and experimental studies using X-rays from a sealed-off tube and monochromatized synchrotron radiation will be given for correlation between TDS and Bragg reflections in mosaic crystals and a nearly perfect germanium crystal.

Recoilless γ-rays called Mössbauer γ-rays are emitted from radioactive isotopes called Mössbauer isotopes. The γ-rays excite Bragg reflection and show diffraction phenomena. The experimental studies related to correlation between γ-ray diffraction and inelastic scattering using recoilless γ-rays are reported.

The experimental technique is applied to nuclear resonance filtering, on which research and development are now progressing.

Contents

Introduction

This paper deals with the correlation between diffraction and inelastic scattering, chiefly thermal diffuse scattering (TDS), of X-rays in mosaic crystals and nearly perfect crystals.

Fluorescent X-rays in a crystal yield Kossel-pattern as well as X-ray TDS and Compton scattering in a crystal yield diffraction pattern similar to Kikuchi-pattern in electron diffraction. The experimental results and theoretical interpretation on diffraction of X-ray TDS will be described in detail.

Intensity of inelastic scattering from a nearly perfect crystal varies when glancing angle of the incident beam varies across the Bragg angle. This phenomenon is considered to be in relation of reciprocal processes of the above mentioned. Experimental result and theoretical discussion will be given on this problem.

Recoilless γ-rays called Mössbaer γ-rays are emitted from radioactive isotopes called Mössbauer isotopes. Nuclear resonance scattering and resonance absorption of the recoiless γ-rays are known as the Mössbaer effect. The γ-rays excite Bragg reflection and show diffraction phenomena. The experimental diffraction studies related to correlation between diffraction and inelastic scattering of recoilless γ-rays will be reported.

The techniques of the X-ray dynamical diffraction as well as Mössbauer γ-ray diffraction are applied to the nuclear resonance filtering of synchrotron radiation, on which research and

development are now progressing.

The aim of this paper is to give a review of these experimental and theoretical studies on coherent effects in inelastic scattering of conventional X-rays, monochromatized synchrotron radiation and Mössbauer recoilless γ-ray for TDS and Bragg reflection in mosaic crystals and nearly perfect crystals. Importance of the problem and observation possibility of the effect in the experiment using synchrotron radiation is stressed. The other purpose of this paper is to make solved and unsolved problem clear, and to show charactaristics and application possibility of this problem for future research and development.

I. Diffraction of Inelastically Scattered X-Rays

1.1. Introduction

This chapter deals with the diffraction of inelastically scattered X-rays, chiefly TDS, in mosaic crystals and nearly perfect crystals.

Fluorescent X-rays yield Kossel-pattern[1],which has been solved theoretically by von Laue[2] using the reciprocity theorem in optics. X-ray TDS and Compton scattering in a nearly perfect crystal yield diffraction pattern similar to Kikuchi-pattern[3,4]. Norman[5] observed diffraction phenomena due to Compton scattering of X-rays in a diamond crystal.

Grenville-Wells[6] first pointed out that TDS X-rays in a crystal are reflected by net planes in the same crystal and diffraction pattern similar to Kossel-pattern will appear in the diffuse scattering. Kainuma[7] first gave the intensity formulae of this pattern and pointed out a new approach to the phase problem. The pattern had been observed[8,9] as diffraction lines across TDS-spots in X-ray film photographs, but the study had not proceeded due to observation difficulty of the faint diffraction line.

Recently, the present authors observed clearly the diffraction line caused by TDS by selecting such a sample crystal as a pyrolytic graphite crystal. The lines depend upon wavelength of the incident radiation, thickness and perfection of specimen crystal, orientation and arrangement of the crystal. Defect line and excess-defect line which look white line and white-black line in the black TDS-spots are caused from mosaic crystal. The excess lines due to anomalous transmission of TDS in a nearly perfect germanium crystal in the Laue geometry has been found for the first time. The progress also owes to such development of X-ray source as synchrotron radiation. The intensities of the lines were measured by means of photographic method and diffractometry.

1.2. Experimental Methods and Results

1.2.1. *Diffraction pattern caused by TDS in mosaic crystal*

Defect lines which look white lines across black TDS spots have been observed in the X-ray film photographs of such mosaic crystals as urea nitrate[10], pyrolytic graphite[11−13], LiF[14,15] and pentaerythritol crystals[16,17]. The perimental methods and the results of the observation will be described in detail.

Unfiltered radiations from a Cu-target or a Mo-target in sealed-off X-ray tubes operated at 30 kV and 10−15 mA were incident with glancing angle θ on flat surface of specimen

crystal in the Bragg geometry as well as in the Laue geometry. Pyrolytic graphite, urea nitrate and pentaerythritol crystals with thickness about 1–2 mm with angular widths about 0.1°– 0.5° of the mosaic domains were chosen as specimens. The specimen crystals were mounted on a goniometer head of a Laue camera. The incident beam was collimated with a tube of length 60 mm and a hole of diameter 0.5 mm.

Figures 1(a) and (b) show X-ray diffraction photographs of a pyrolytic graphite crystal taken with unfiltered radiations from Cu-target incident on the flat surface parallel to the (001) plane at glancing angles of 13.3° and 15.3°, respectively, in the Bragg case. Since the glancing angles are close to the Bragg angle $\theta_B = 13.3°$ for the 002 reflection of CuKα X-ray, the large diffuse spot A and the small one B are due to the TDS of Kα and Kβ X-rays near the 002 reciprocal-lattice point, respectively. The spot E is due to the incident beam penetrating the crystal and thin lead sheet before a film. The sharp long defect line D is clearly seen across the middle of the diffuse spot A and the Laue spot C. In the figures, the deviation angles between the spot A and the line D and between the spot C and the line D are the same. They are nearly equal to the deviation angle $\Delta\omega$ of the glancing angle θ from the Bragg angle θ_B. The origin of the defect line can be explained as follows using Fig. 2, which illustrates schematically the propagation of X-rays in the real space. We suppose the crystal surface parallel to the reflecting net planes. The deviation angle $\Delta\omega$ of the incident beam from the Bragg angle is less than a few degrees. We assume further that inelastic scattering and diffraction are kinematical. This means that a single Bragg reflection of inelastically scattered X-ray is taken into consideration. A Laue spot LS is caused in the direction with scattering angle $2\theta_B + 2\Delta\omega$ by the mirror reflection of the incident white radiation. The intensity maximum in a TDS diffuse spot DS is observed in the direction with scattering angle close to $2\theta_B$. If a cone of the TDS is incident on the 002 reflection planes with the Bragg angle θ_B in the crystal, the direction of the TDS is changed by the 002 reflection in the crystal. Thus the defect line DL is caused in the diffuse spot and observed in the middle between the Laue spot and the diffuse spot. Figs. 3(a), (b) and (c) show the diffraction photographs of a pentaerythritol crystal taken at angles $\theta = 9.6°$, 10.1° (θ_B for CuKα X-ray) and 10.6° from the
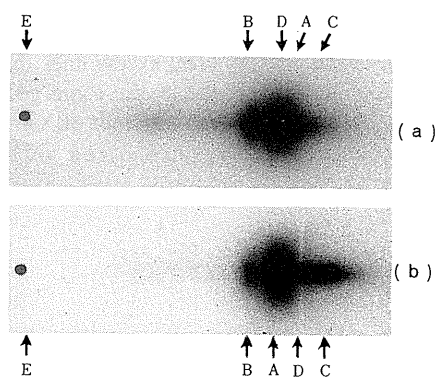

Fig. 1. X-ray diffraction pattern of a pyrolytic graphite crystal in the symmetric Bragg geometry taken at glancing angle $\theta = \theta_B + \Delta\omega$, (a) 13.3° and (b) 15.3° using collimated unfiltered radiation from Cu-target.
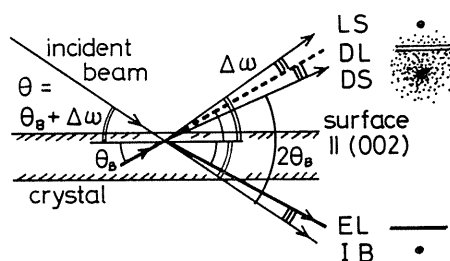

Fig. 2. Propagation direction of X-rays in a mosaic crystal. IB, incident beam; DL, defect line; DS, thermal diffuse scattering; LS, Laue spot.
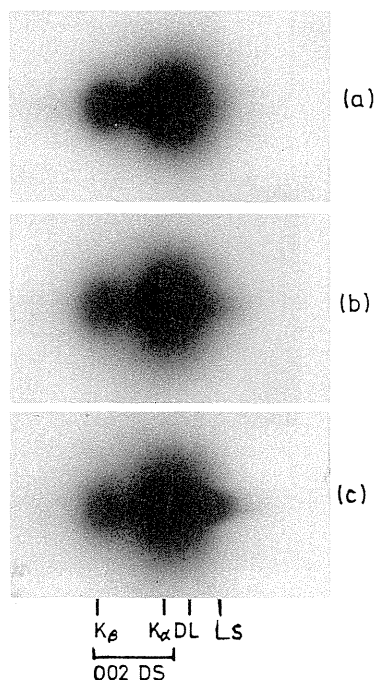
(a)

(b)

(c)

K_β K_α DL LS

002 DS

Fig. 3. Diffraction photograph of pentaelythri-
tol crystal. DL, white line; DS, TDS
spot; LS, Laue spot. Angle θ, (a) 9.6°,
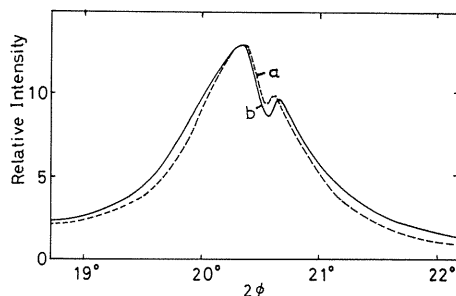(b) 10.1° and (c) 10.6°. Laue case.

Fig. 4. a, Theoretical curve corrected for source
size and collimator system. b, ex-
perimental curve.

reflecting (002) plane perpendicular to the crystal surface in the Laue case. The origin of the defect lines and the excess lines in Figs. 3 can be explained in the same way as those in Fig. 2. From the above figures, we can understand qualitatively the origin of the defect line across the TDS spot and the excess line near the incident beam spot, respectively and the θ-depend-ence or crystal orientation-dependence of those lines.

Intensity curves across defect lines were measured by densitometry of the diffraction photographs of the pentaerythritol crystal as shown in Fig. 3. Fig. 4 shows the experimental intensity curve across the defect line in the photograph taken at $\theta = 10.3°$ at room tempera-ture. The solid line shows an experimental curve. The dotted line shows a theoretical curve corrected for source size and collimator system. The calculation was performed on the basis of the secondary extinction theory in section 1.3.1. The contrast and the width of the line ob-tained in the Laue case were compared successfully with those calculated on the assumption that the angular distribution of the mosaic domains is Gaussian. Temperature dependence of the line and the diffuse spot were ascertained also. Although, disagreement between those of observation and calculation were found in the Bragg case.

1.2.2. *Diffraction pattern caused by TDS in nearly perfect crystal*

(1) Bragg case

A black line which the present authors call an excess line, in place of a white line, was
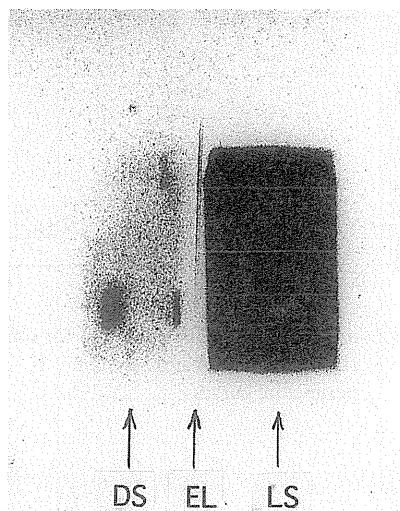
Fig. 5. Diffraction photograph of a calcite crystal. DS, thermal diffuse spot; EL, excess line; LS, Laue spot.
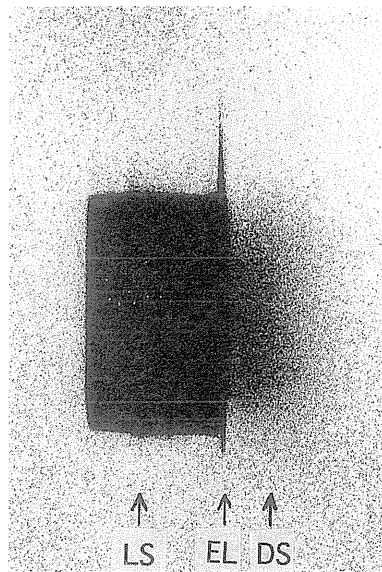
Fig. 6. Diffraction photograph of a germanium crystal. DS, thermal diffuse spot; EL, excess line; LS, Laue spot.

observed first across the 200 diffuse spot of a calcite crystal in a X-ray film photograph[18] using unfiltered radiation from a copper target in a sealed off X-ray tube operated at accelerating voltage 30 kV and 10 mA and X-ray film. The specimen calcite crystal has a cleft surface parallel to the (100) planes of area 10 mm × 10 mm and thickness 2.5 mm. Optical system of the Laue camera was the same as mosaic crystals'. Fig. 5 shows the diffraction photograph taken at a glancing angle $\theta = 13.6°$, which is close to the angle $\theta_B = 13.24°$ for the 200 reflection of Cu-Kβ X-ray, in the Bragg case. The dark spot is the Laue spot caused by the 200 mirror reflection of the white radiation. The diffuse spot was caused by the TDS of Kβ X-ray near the 200 reciprocal lattice point. A sharp black line is clearly seen across near the middle between the diffuse spot and the Laue spot. The excess line was observed under the following experimental conditions. (1) The surface of the crystal is parallel to the reflecting net plane in the crystal. (2) The deviation angle $\Delta\omega = \theta - \theta_B$ of the incident beam from the 200 Bragg angle θ_B is within one degree. (3) The specimen crystal has a large value of normal absorption coefficient of CuKβ X-rays, 190cm^{-1}. (4) The specimen is ideally perfect. (5) The X-ray beam is incident on an edge of the crystal. Similar black lines were observed across the thermal diffuse spots on the film photographs of an ideally perfect germanium crystal[19] in the Bragg geometry using unfiltered white radiation from a copper target in a sealed-off X-ray tube and optical system of the same Laue camera. Fig. 6 shows the X-ray film photograph of a germanium crystal taken at glancing angle $\theta = 13.15°$, which is close to the angle $\theta_B = 13.65°$ for the 111 reflection of Cu-Kα radiation, in the Bragg case. The germanium specimen thickness is about 2 mm. A long sharp line seen between Laue spot and diffuse TDS spot is the excess line. The origin of the excess line is qualitatively explained under the above mentioned condition using Fig. 7, which shows a schematic illustration of the
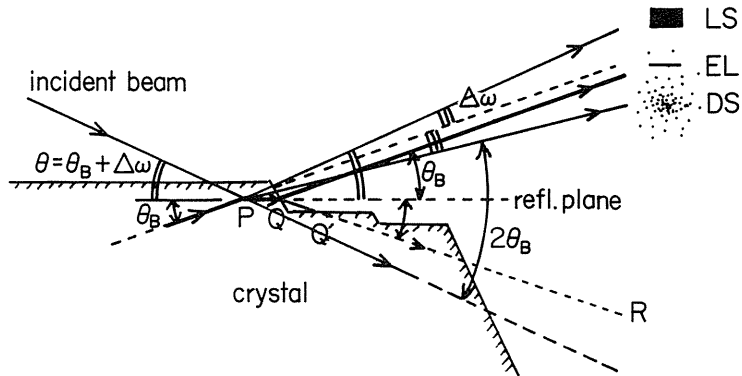
Fig. 7. Ray paths of the beam incident on an edge of a crystal, TDS with the intensity maximum DS, radiations forming Laue spot LS and the excess line EL.
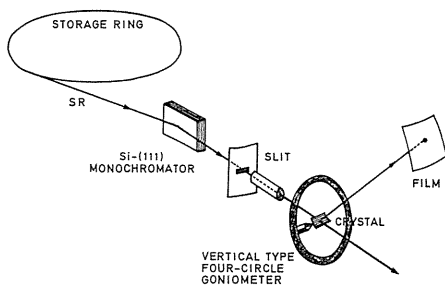

Fig. 8. Instrumental arragement at PF, BL-10A.
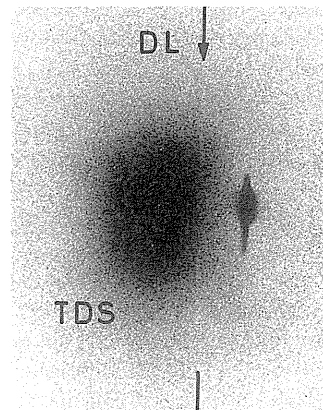
Fig. 9. Diffraction photograph of a germanium crystal in Bragg geometry, $\Delta\omega = +0.4°$.

ray paths related to the TDS, the Laue spot LS and the excess line EL. If a cone of the TDS incident on the reflecting net plane at point P with the angle θ_B inside the crystal, the energy will be transmitted through the crystal preferentially along the reflection net plane from point P to Q on the crystal surface. This phenomenon is attributed to the Borrmann effect[20] or anomalous transmission. The strong intensity of the excess line is due to the small value of X-ray anomalous absorption coefficient.

Thereafter, the experimental method of observing the diffraction line of TDS was improved using monochromatized synchrotron radiation of wavelength 1.54Å and film for cosmic-ray observation. Fig. 8 shows the instrumental arrangement installed at the Photon Factory (PF), beam line (BL) 10 A of the National Laboratory for High Energy Physics (KEK). Advantages of synchrotron radiation are easy choice of wavelength, collimation and strong intensity of the monochromatized radiation. Synchrotron radiations with horizontal and

vertical divergences less than 0.5 mrad were monochromatized by the silicon 111 reflection which has energy resolution $\Delta E/E$ about 5×10^{-5}. The monochromatized radiation was collimated with a collimator and slits of 0.25 mm and 0.37 mm in heights and 3.0 mm in width.

Defect line and defect-excess line in place of excess line were observed[21] in the diffraction photographs of the 220 TDS from nearly perfect germanium crystal in the Bragg geometry, when collimated and monochromatized synchrotron radiation was incident on the flat surface far from an edge of the crystal. Fig. 9 shows an example of diffraction pattern from a germanium crystal with the (110) surface in the symmetric Bragg geometry. The wavelength is 1.54Å and the crystal thickness is 0.47 mm. The crystal was set near but off the 220 Bragg position. The 220 Bragg reflection was not excited strongly. The angular deviation is $+0.4°$. A diffuse spot TDS is due to the 220 thermal diffuse scattering and a sharp spot is due to tail of the 220 Bragg reflection. Just in the middle of the TDS and Bragg spots, a long defect diffraction line indicated by DL is observed. The line has a slightly excess-defect structure where the excess part is always on the lower angle side. When $\Delta\omega = 0$, the Bragg spot and the diffraction line are superposed approximately on the center of TDS spot. The TDS spot is left fixed, when $\Delta\omega$ is changed. The Bragg spot is displaced by $2\Delta\omega$ from the position for $\Delta\omega = 0$ and the diffraction line is displaced by $\Delta\omega$. These behaviors of patterns are the same as the previous observation in the Bragg case[18]. In the Bragg case, the Bragg-reflected spot moves with the crystal like a mirror-reflected beam, while the Bragg spot is almost fixed in the Laue case. Another photographic observation was made for smaller $\mu D = 1.3$, where μ is absorption coefficient, wavelength is 1.120Å and $D = 0.083$ mm. The results similar to the case of 1.50Å were obtained also. The origin of the defect line in the Bragg case were qualitatively predicted by Kainuma, who gave the dynamical diffraction theory of TDS without absorption effect. The present authors also extended the dynamical diffraction theory of TDS including absorption effect. The theoretical calculation,which will be published later, agrees qualitatively with the experimental result.

(2) Laue case

The excess line of germanium crystals[22,23] in Laue geometry was found first using monochromatized synchrotron radiation of wavelength 1.54Å and film for cosmic-ray observation. Parallel plate germanium crystal (specimen A) with thicknesses about 0.10 mm and surfaces parallel to the (111) plane polished and etched chemically to take off imperfect surfaces was used. The full widths at half maximum (FWHM) of the 111 rocking curve of the specimen A in the Bragg geometry is about $16''$, which is close to the values of the perfect crystal. The crystal plate was mounted on a goniometer head on the vertical-type (diffraction plane is vertical) four circle diffractometer. Synchrotron radiation with horizontal and vertical divergences less than 0.5 mrad were monochromatized by the silicon 111 reflection which has energy resolution $\Delta E/E$ about 5×10^{-5}. The monochromatized radiation was collimated with a collimator and slits of 0.25 mm and 0.37 mm in heights and 3.0 mm in width. The radiations of wavelength 1.15Å and 1.54Å were incident on the germanium crystal in the Laue geometry. Diffraction patterns were observed by Sakura X-ray films for cosmic ray observation, set perpendicularly to the diffracted beam. The film-specimen distances were $45 \sim 49$ cm. Figs. 10(a)—(c) show the diffraction photographs of the specimen A at room temperature taken at incident angles $\psi = 23.05°$, $22.65°$, and $22.05°$, respectively, which are close to the angle $\theta_B = 22.65°$ for the 220 reflection of the 1.54Å radiation. Exposure time was about one hour at electron currents about 100—200 mA. In the figures a large diffuse spot LS is the reflection spot due to weak contaminated white radiation and due to tail of the Bragg reflection, a long sharp line El composed of strongly black and weakly white lines is the excess line. In the above photographs, we can see that variation of crystal orientation affects the intensity of the thermal diffuse spot and that small angular variation in the crystal orientation dose not

move the direction of the intensity maximum of the diffuse spot. The peak intensity of the excess line decreases with increasing $|\Delta\omega|$, where $\Delta\omega$ is the deviation angle of ψ from the Bragg angle θ_B. When $|\Delta\omega|$ increases, the line disappears but the spot is observed still weakly. The width of the excess line does not vary with $\Delta\omega$. Fig. 11 shows a schematic illustration of ray-path of radiation scattered in the germanium specimen in the Laue case. The excess line ELH near the incident beam spot and the excess line EL across DS spot are caused by the ray which propagate from P to Q along the reflecting net plane and split into

(a)

(b)

(c)

LS   EL   DS

Fig. 10. Photograph of a germanium specimen with thickness 0.1 mm showing diffraction pattern near the 220 thermal diffuse spot DS of 1.54Å radiation in the Laue case. EL, excess line; LS, Laue spot.
(a) $\Delta\omega = \psi - \theta_B = 0.4°$, (b) $\psi = \theta_B = 22.65°$, (c) $\Delta\omega = 0.6°$.
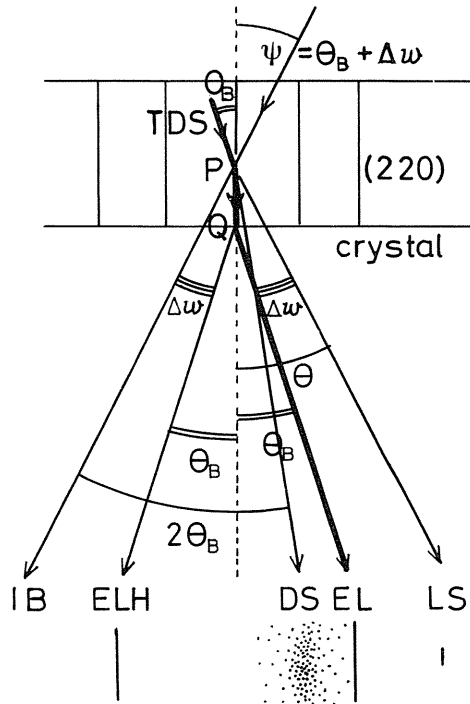
Fig. 11. Ray-paths of radiations in a thick perfect crystal in the symmetric Laue geometry.

two parts at Q propagating to ELH and EL. Intensity curve across the lines depends on wavelength of incident radiations. Fig. 12 shows the diffraction photograph of the germanium specimen at room temperature taken at $\psi = 16.31°$ in the Laue case, which is close to the Bragg angle 16.71° for the 220 reflection of the 1.15Å radiation. Exposure time and electron current were 1.0 hour and 170 mA. In these figures, we can see that the excess-defect line composed of weak black line beside white line appears. The intensity contrast of the excess-defect line to the TDS background is much lower than that of Figs. 10(a)—(c). The white line in the excess-defect line appears at scattering angle always slightly higher than the black line. Figs. 13(a) and (b) show the diffraction photographs of the germanium specimen A at room temperature taken at $\psi = 23.05°$ and 22.25°, respectively. The wavelength of the incident beam through the slit of size 0.25 mm × 3.0 mm was 1.540Å. Exposure time and electron current were one hour and 160—180 mA. We can see a sharp black line ELR near the shadow of an incident beam stopper. The deviation angle between the propagating directions of the incident beam and the excess line ELR is equal to $\Delta\omega = \psi - \theta_B$, where θ_B is the Bragg angle for the 220 reflection of the 1.54Å radiation. The line is parallel to the (220) reflecting
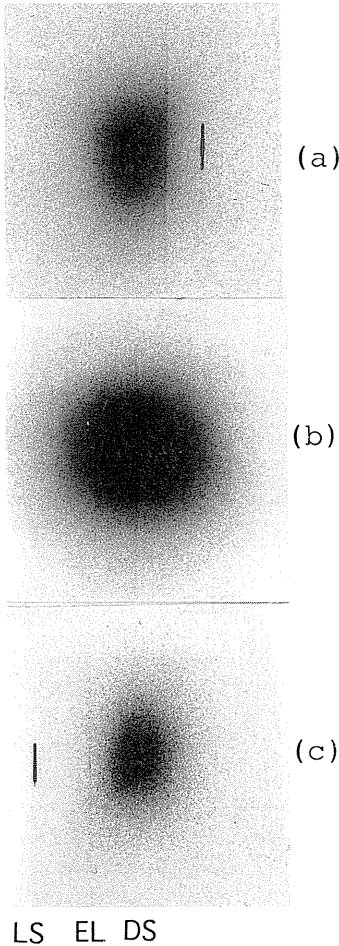

Fig. 12. Photograph of germanium specimen A with thickness 0.1 mm showing diffraction pattern near the 220 thermal diffuse spot DS of 1.15Å radiation in the Laue case. EL, excess line; $\psi = 16.31°$, $\Delta\omega = -0.4°$.
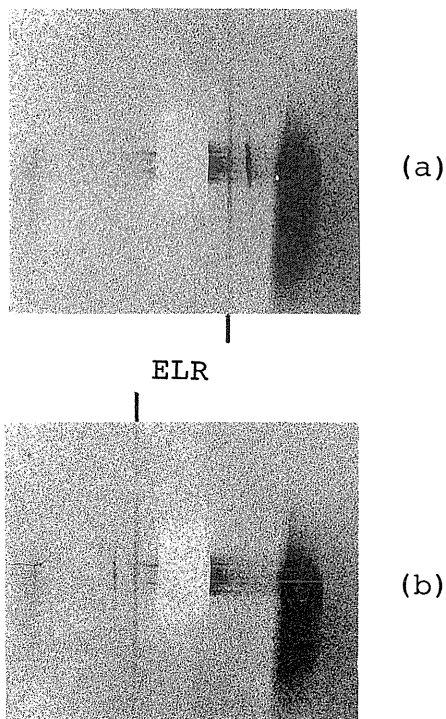

Fig. 13. Photograph of specimen A showing the excess line ELR near white shadow of the incident beam stopper. Wavelength of the incident beam 1.54Å. Silt size 0.25 mm × 3.0 mm. (a) $\psi = 23.05°$, $\Delta\omega = 0.4°$; (b) $\psi = 22.25°$, $\Delta\omega = -0.4°$.

plane. The similar excess lines near the incident beam spot were observed on the film photo-graph of the same specimen by using the radiation of wavelength 1.150Å. The diffraction pattern of TDS similar to that of the germanium crystal was observed across the 220 TDS spot of perfect silicon crystals with thickness about 0.1 mm−0.3 mm and the surfaces parallel to the (111) plane in the Laue geometry. If we use an imaging plate[24,25] in place of film photograph or scintillation detector, we can clearly observe very long and sharp excess line owing to the high position-resolution and wide dynamic range of the imaging plate. Fig. 14 shows an example of the excess line on an imaging plate. The diffraction pattern of a germa-nium crystal with thickness 0.17 mm set at $\Delta\omega = 0.3°$ from the Bragg angle of the 220 reflec-tion in the Laue geometry was taken using monochromatized 1.54Å synchrotron radiation.

The results of the photographic observation are summarized as

(1)   The excess line EL across the 220 TDS spot as well as the excess line ELR near the incident beam spot were observed clearly. They depend on the crystal orientation, the wave-length of the incident beam and the crystal thickness.

(2)   The excess lines EL and ELR can be observed under the following conditions. Per-fection of the crystal structure and absorption are very high. the TDS intensity is strong enough to be observed.
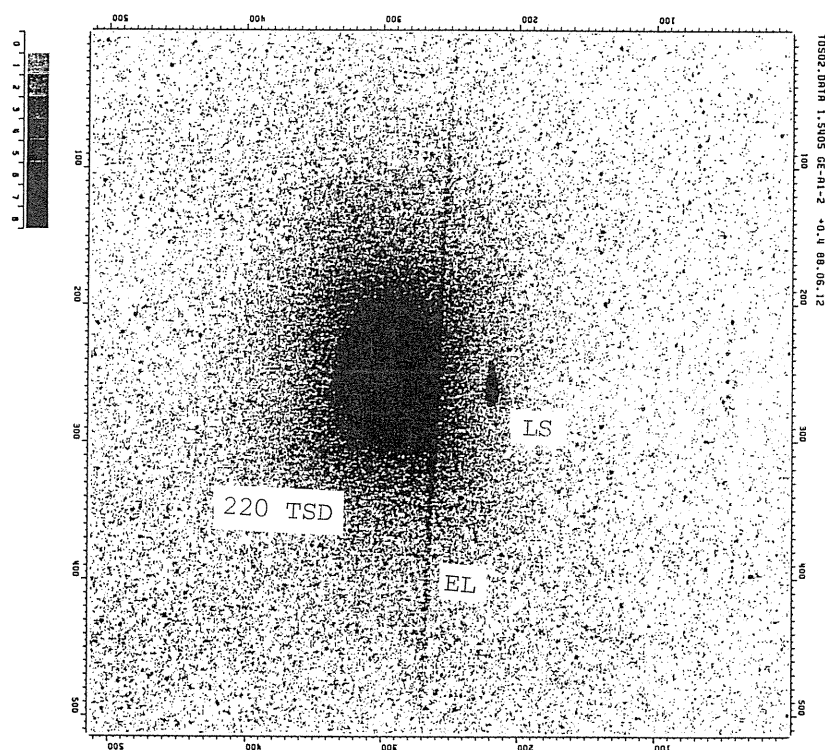

Fig. 14. The diffraction pattern on an imaging plate of a germanium crystal with thickness 0.17 mm set at $\Delta\omega = 0.3°$ from the 220 Bragg angle for the 1.54Å synchrotron radiation taken at PF, BL-10A. A long sharp line is the excess line. Large diffuse spot is the 220 TDS spot. Small spot is the Laue spot due to contaminated white radiation.

(3)   The intensity profile of the EL line varies from excess to excess-defect according as the specimen thickness decreases.

(4)   The intensity of the ELR line depends on the specimen thickness as well as wavelength of the incident beam. However, the intensity profile of the ELR line is always excess and symmetric in shape.

The experimental work mentioned above is rather qualitative. Quantitative observations of the diffraction pattern have been successfully performed by means of counter diffractometry[24,26,27]. Intensity measurements of the diffraction patterns using imaging plate as well as scintillation counter were carried out[24] at BL-10A with the experimental arrangement shown in Fig. 8. Temperature dependence of the above mentioned excess line of the germanium crystal was ascertained also. Fig. 15 schematically illustrates the experimental arrangement of the triple-crystal diffractometry system installed at BL-15C of the Photon Factory. The system is of the vertical type in which all diffraction planes are vertical. The polarization of the synchrotron radiation is always perpendicular to the normals of the Bragg reflecting planes. A parallel plate of germanium single crystal with the (111) surface polished and chemically etched was used as a specimen. The size of the crystal surface was about 5×5 mm^2, and the thickness is 0.18 mm. Perfection of the specimen was ascertained from measurement of the rocking curve of the 220 reflection in the Laue case. The rocking curve had a symmetric profile with a full width at half maximum (FWHM) of 5.8″, which was close to the theoretical value of 4.9″ for an absorbing perfect crystal.

Synchrotron radiation with horizontal and vertical divergences less than 2′ was monochromatized to $\lambda = 1.540$Å by the 111 symmetric reflection of the silicon-crystal monochromator M. The monochromatized beam, led into the collimator C of a grooved silicon crystal, was made tailless by 5-times-consecutive symmetric 220 Bragg reflections. The nearly plane-wave beam was then incident on the specimen crystal S, which was mounted on a goniometer head and set near the 220 Bragg position in the Laue arrangement. The scattered beam was analyzed by the second grooved crystal A, used as an angle-resolving analyzer and of the same structure as the collimator. After the same process as in C, the angle-resolved beam entered the scintillation counter D. The beam intensity was measured by a typical counting system with a pulse-height analyzer. The incident beam was always monitored by the ionization chamber IC during the measurements. The dimensions of the three-crystal arrangement were about 75 cm between the collimator and the specimen, and about 9 cm between the specimen and the analyzer. The cross section of the beam was 1.5×1.7 mm^2 on the specimen crystal. The beam divergence was about 10″ in the horizontal plane and 4″ in the vertical plane.
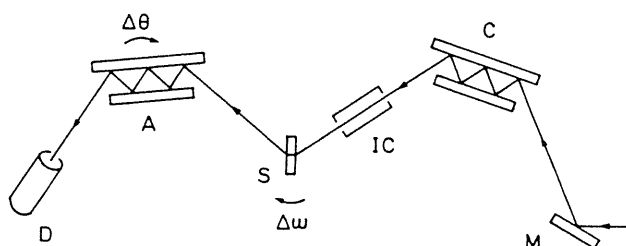

Fig. 15. The triple-crystal diffractometer, consising of a silicon (111) monochromator M, collimator C and analyzer A of silicon grooved crystals with (220) surfaces, specimen crystal S, scintillation counter D, and ionization-chamber monitor IC. All ray paths lie in the same vertical plane, to which the polarization of radiation is perpendicular.

The specimen and the analyzer crystals were rotated by tangential screws with an accuracy of 0.1″. To obtain the intensity profile of the TDS in which an excess line is expected to appear as a peak, an angle-resolved measurement was made across the 220 TDS spot by rotating the analyzer step-wise with the specimen crystal fixed near the 220 Bragg position. A reflection curve for the arrangement in Fig. 15 observed with an optically flat mirror shows that the angular resolution in the diffraction plane is about 4″. The resolution function perpendicular to the diffraction plane is independent of the angle of scattering, since the monochromator, analyzer, and specimen crystals are nearly perfect. These results ensure that the resolution function is good enough to resolve the present peak. Scattering from surface imperfections does not disturb the intensity measurements, since all scattering except anomalous transmission is strongly absorbed in penetrating the specimen. The analyzer was scanned in the plane perpendicular to the [112] axis of the specimen. The scanning range was $\pm 50''$ around the diffraction peak and the step size was 1.5″. The direction of the scattered X-rays is determined by the rotation angle of the analyzer. The angle is indicated by the angular deviation $\Delta \theta$ from the intensity maximum of the 220 Bragg peak when the specimen is just on the Bragg position. The angle $\Delta \theta$ was taken to be positive for increasing scattering angle.

Figures 16(a)–(c) show measured profiles of diffuse scattering plotted against $\Delta \theta$ for
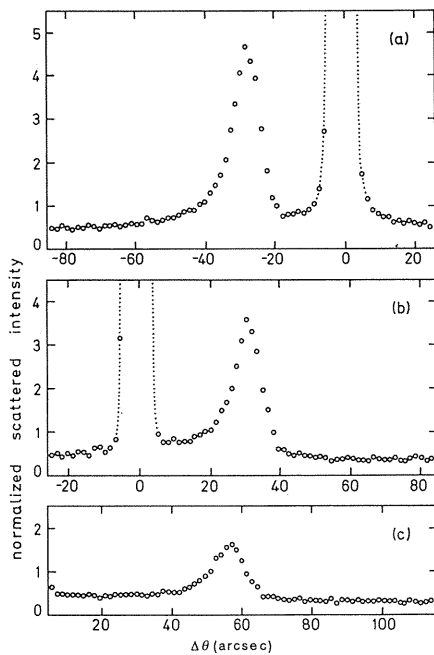
Fig. 16. Observed intensity profiles of excess lines in the 220 TDS spot of a germanium crystal for various orientations. (a) $\Delta \omega = -30''$, (b) $\Delta \omega = 30''$, (c) $\Delta \omega = 60''$. The ordinates indicate scattered intensities normalized by the monitor count of the incident beam. Actual count of the peak maximum in (a) is about 2×10^3 per 50 s. Dotted curves due to tail of the 220 Bragg reflection.
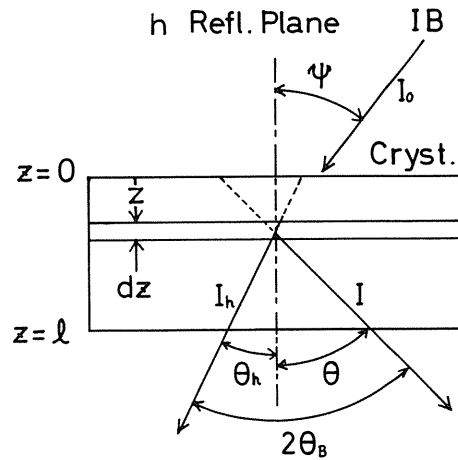
Fig. 17. Schematic illustration of TDS diffraction in the Laue case.

various crystal orientation indicated by the angular deviation $\Delta\theta$ from the 220 Bragg position. The intensity is normalized by the monitor count of the incident beam. Diffraction peaks are observed in all figures, where their heights decrease as $\Delta\omega$ increases but the widths are almost fixed. Actual counts at the diffraction peaks were about $3 \times 10^2 - 2 \times 10^3$ per 50 s. The saturated peaks in Figs. 16(a) and (b) are due to the tails of the 220 reflections far from the Bragg position. Their peak heights are about 50 times those of the diffraction peaks. The backgrounds of the profiles change very slowly with $\Delta\theta$ and are roughly constant. The background intensity of TDS, except at the peak positions, is decreased by normal absorption to the noise level, since the specimen crystal is thick in the present Laue case. This contrasts with the measurements in the Bragg case.

Some characteristics of the diffraction peaks observed in the experiment are summarized as follows.

(1)   The angular displacement of the peak position, as the specimen crystal is rotated, is equal to the rotation angle $\Delta\omega$. This coincides with the previous result of photographic observations of the excess lines. Diffuse X-rays giving rise to the observed peaks correspond to almost exact satisfaction of 220 Bragg condition.

(2)   The FWHM's of the peaks are about 10″. This value is of the same order as the 220 reflection width calculated from dynamical diffraction theory.

(3)   The shapes of the peak profiles are slightly asymmetric. The gradient of every peak is always steeper on the high-angle side than on the low-angle side.

(4)   The peak height above the background level is roughly estimated to be proportional to the inverse square of the deviation angle $\Delta\omega$ and thus to the inverse square of the phonon wave vector from the 220 reciprocal-lattice point. This implies that the peak height is proportional to the TDS intensity. The diffraction peak is formed by TDS.

1.3.   Theory and Comparison with Experiment

1.3.1.   *Secondary extinction theory for diffraction of TDS in mosaic crystal*

A simple model which takes a single Bragg reflection of inelastically scattered X-ray wave into consideration, i.e., Kinematical diffraction, is used so far to explain qualitatively the origin of the white line. Here, quantitative explanation of the cause of the intensity dip across the white line will be described in detail.

We deal with the Laue case in which the propagation of X-rays in parallel plate crystal of thickness ℓ is shown in Fig. 17. A monochromatic unpolarized collimated beam IB of intensity I_0 is incident on the h net plane normal to the surface at glancing angle $\psi = \theta_B + \Delta\omega$. Since we don't deal with the case when the Bragg reflection of the incident beam occurs, the deviation angle $\Delta\omega$ is restricted as $\Delta\omega \gg \Delta\theta_B$. The incident beam is attenuated first by ordinary absorption within thickness z under the entrance surface of the crystal. Thermal diffuse scattering occur in the z-$z + dz$, and has angular divergence in the diffuse intensity distribution as shown in photographs. A part of them is incident on the reflecting net plane h at the Bragg angle. Considering secondary extinction for the diffraction of the TDS similar to that introduced into the diffraction of elastically scattered X-rays by Hamilton and Zachariazen, we have

$$\frac{dI}{dz} = -\frac{(\mu + \sigma)}{\cos\theta}I + \frac{\sigma}{\cos\theta_h}I_h + \frac{I_0 S}{\cos\theta}e^{-\mu z/\cos\psi}, \tag{1}$$

$$\frac{dI_h}{dz} = \frac{\sigma}{\cos\theta}\,I - \frac{(\mu+\sigma)}{\cos\theta_h}\,I_h + \frac{I_0 S_h}{\cos\theta_h}\,e^{-\mu z/\cos\psi}\,, \tag{2}$$

where $I = I(z,\theta)$ and $I_h = I(z,\theta_h)$ defined in Fig. 17. are TDS intensities at the depth z. Both θ and θ_h are equal to or close to θ_B in the present case. Notations σ and μ are reflectivity and absorption coefficient, respectively. The first term in the right of eq. (1) means the decrease of I by absorption and reflection within the thickness dz. The second term means the increase of I by reflection of I_h. The third term means the increase of I due to TDS generated in the volume (unit area)xd$z$/cosψ irradiated by the incident beam with intensity decreased by absorption for the ray-path length in the crystal. Both cosθ and cosθ_h in the third terms of (1) and (2) must be cosψ in the correct expression, however, become approximately equal to cosψ with error less than one percent, since the $\Delta\omega$ is less than one degree and ψ is close to θ and θ_h. Notation S is the intensity of TDS generated per unit intensity of the incident beam and per unit volume of the specimen. It must be noted that I_h and S_h are defined for the direction near the IB. We treat inelastic scattering including TDS kinematically. This means to assume that inelastic scattering occurs in each multilayers of thickness dz, and that third terms in eqs. (1) and (2) play roles of radiation source in the crystal. The third term in eq. (2) can be neglected in the case of TDS, since TDS's S_h is negligibly small in the small angle scattering in comparison with S. The term, however, can not be neglected in such inelastic scattering as Compton scattering and fluorescent emission. The solution of eqs. (1) and (2) is expressed as

$$I = I^0 - I_{DL} + I_{EL}\,. \tag{3}$$

The first term denotes the intensity of TDS, when $\sigma = 0$, i.e. no reflection occurs. The second and the third terms denote the defect line in the TDS spot and the excess line near the incident beam, respectively. Their formulas are given as follows.

$$I^0 = \frac{I_0 S}{\mu(1-\cos\theta/\cos\psi)}\,[\exp(-\mu\ell/\cos\psi) - \exp(-\mu\ell/\cos\theta)]\,, \tag{4}$$

The formula of I_h^0 is obtained by insertion of S_h and θ_h in place of S and θ in eq. (4), respectively.

$$I_{DE} = \frac{I_0 S}{\mu}\,[-4y\,\frac{(\rho-\gamma)}{(1-\rho)}\,M_1 M_2 \exp(-\mu\ell/\cos\psi) + (1 + \frac{D_2}{D})\,M_1 \exp(\eta_1\ell)$$

$$+ (1 - \frac{D_2}{D})\,M_1 \exp(\eta_2\ell) - \frac{1}{(1-\rho)}\exp(-\mu\ell/\cos\theta)]\,, \tag{5}$$

$$I_{EX} = \frac{I_0 S_h}{\mu}\,\frac{2y}{D}\,\gamma^2\,[2DM_1 M_2 \exp(-\mu\ell/\cos\psi)$$

$$+ M_1 \exp(\eta_1\ell) - M_2 \exp(\eta_2\ell)]\,, \tag{6}$$

with

$$\eta_{1,2} = \frac{-\mu}{2 \cdot \cos\theta} \left(D_1 \pm D\right),$$

$$D_{1,2} = (1 + y)(1 \pm \gamma), \quad D = \left(D_2 + 4\gamma y^2\right)^{1/2},$$

$$y = \frac{\sigma}{\mu}, \quad \gamma = \frac{\cos\theta}{\cos\theta_h},$$

$$M_{1,2} = \left(D_1 \pm D - 2\rho\right)^{-1}, \quad \rho = \frac{\cos\theta}{\cos\psi_h}. \tag{7}$$

Figure 4 compares the experimental intensity curve across the defect line of the photograph taken at $\psi = 10.3°$ at specimen temperature 273 K in the Laue case with the calculation which was performed using the above equations with correction for source size and collimator system.

For the Bragg case, intensity formulas corresponding to eqs. (3)—(7) have been obtained also. The formulas were applied to explain a white (defect) line which appeared as a dip in intensity distribution in the 200 diffuse scattering from a Cu-Al disordered crystal[28] at room temperature in the Bragg geometry by using both photographic and counter method. The diffuse scattering is caused by the static displacement of atoms as well as the thermal motion of atoms. The observed contrast of the line agreed quantitatively well with that calculated.

1.3.2. *Dynamical diffraction theory for nearly perfect crystal*

The experimental result described above is now compared with calculation based on the dynamical theory. We consider the propagation of X-ray waves in the symmetric Laue geometry of an ideally perfect crystal of thickness D as shown in Figs. 18(a) and (b). A monochromatic collimated beam of intensity I_0 in σ polarization is incident on the net planes at glancing angle $\psi = \theta_B + \Delta\omega$, where θ_B is the Bragg angle. Since we deal with Bragg
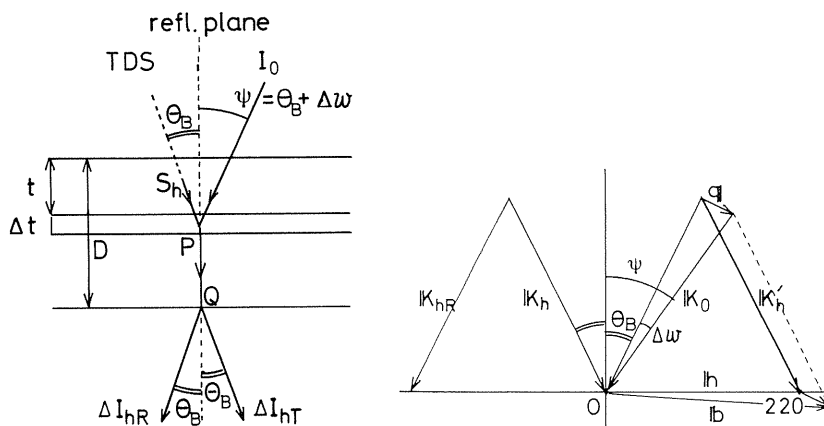

Fig. 18. (a) Ray paths related to diffraction near the 220 reciprocal lattice point.
(b) Wave vectors in the reciprocal space.

reflection of the TDS near a reciprocal lattice point, the deviation angle $\Delta\omega$ is much smaller than θ_B, but larger than the beam divergence and $2\Delta\theta_B$, i.e., FWHM of the rocking curve of the Bragg reflection. Rough estimation of the deviation angle generally is $0.1° < |\Delta\omega| < 1°$. The incident beam is attenuated first by ordinary absorption during propagation, with no Bragg reflection, from the entrance surface to the depth t in the crystal. Thermal diffuse scattering occurs in the layer $t \sim t + \Delta t$ into a direction near the h reflection. A part of the TDS in the angular region $2\Delta\theta_B$ is incident on the h net planes at the Bragg angle and excites the Bragg reflection. The transmitted and reflected TDS waves interact dynamically to form two waves which are strongly or weakly absorbed according to whether they have antinodes or nodes on the reflecting atom planes. This causes an anomalous absorption or transmission, well known as the Borrmann effect. The waves with nodes at the atom planes propagates through the crystal of thickness $D\text{-}t$ with anomalously low absorption. Under the exit surface of the crystal, the intensities of the transmitted and the reflected beams, i.e. ΔI_{hT} and ΔI_{hR}, respectively, will be observed across the thermal diffuse spot and near the incident beam spot, respectively. The intensity of the transmitted beam is given by

$$\Delta I_{hT} = I_0 S_h \exp(-\mu t/\gamma)\,\frac{\Delta t}{2D}\left[\begin{array}{l} \dfrac{1}{2}(1 - \dfrac{W}{\sqrt{1+W^2}})^2 \\[2mm] \quad \times \exp(-\dfrac{\mu}{\gamma}(D-t)(1 - \dfrac{\kappa_0}{\sqrt{1+W^2}})) \\[2mm] + \dfrac{1}{2}(1 + \dfrac{W}{\sqrt{1+W^2}})^2 \\[2mm] \quad \times \exp(-\dfrac{\mu}{\gamma}(D-t)(1 + \dfrac{\kappa_0}{\sqrt{1+W^2}})) \end{array}\right] , (8)$$

where μ is the normal linear absorption coefficient, and $\gamma = \cos\theta_B$. The first and the second terms in the largest brackets of eq. (8) correspond to the standing-waves belonging to the branch 1 and 2 of the dispersion surfaces which have nodes and anti-nodes, respectively, at the atom-planes. Notations, κ_0 and W are given as

$$\kappa_0 = (\phi_{hi}/\phi_{0i})\,(|\phi_{hr}|/\phi_{hr}) \tag{9}$$

and

$$W = (\theta - \theta_B)\sin(2\theta_B)/|K\phi_{hr}| , \tag{10}$$

where ϕ_{hr} and ϕ_{hi} are real and imaginary parts of the h Fourier coefficients of complex electric susceptibility with $\phi_h = (e^2/mc^2)\lambda^2 F_h/\pi v_a$, where v_a is unit cell volume. The notation K is the polarization factor $\cos(2\theta_B)$. The parameter θ is the angle between the reflecting plane and the propagating direction of the transmitted waves under the exit surface of the crystal. (In the ordinary dynamical theory, θ is defined to the incident beam direction. In this paper, it is convenient to use the above definition of θ). The factor S_h, the intensity of TDS per unit intensity of incident X-ray, is given as

$$S_h = (I_e/I_0) \, k_B T \, b_h^2 |G_h|^2 [\Omega^{-1}(q)]^{bb} \delta V/(v_a^2 q^2) \tag{11}$$

with

$$G_h = \sum_k f_k(b_h) \exp\left(-M(b_h)\right) \exp\left(-i b_h r_k\right)$$

and

$$b_h = K_h' - K_0 = h + q = q_h \, .$$

where K_0, K_h and q are the wave vectors of the incident wave, the thermally scattered wave and the lattice wave in the crystal as shown in Fig. 18(b). The G_h is the structure factor corrected with temperature factor. The factor $[\Omega^{-1}(q)]^{bb}$ is replaced by Jahn's equation by using elastic constants. The δV is the scattering volume of the specimen.

The intensity of the reflected beam ΔI_{hR} is given by

$$\Delta I_{hR} = I_0 \exp\left(-\mu t/\gamma\right) S_h \left(\Delta t/D\right) \frac{1}{2} \frac{1}{(1+W^2)}$$

$$\times \exp\left(-\frac{\mu}{\gamma}(D-t)\right) \cosh\left(\frac{2\kappa A'(D-t)}{\sqrt{1+W^2}}\right), \tag{12}$$

$$A' = \pi k |\phi_{ht}|/\gamma \, , \tag{13}$$

where k is the wave number of the thermally scattered X-ray wave, $\kappa = \phi_{hi}/\phi_{hr}$ and then $\kappa A' = \pi k |\phi_{oi}| |\kappa_0|/\gamma = \mu |\kappa_0|/2\gamma = \Delta\mu/2\gamma$.

Integration of eqs. (8) and (12) leads to

$$I_{hT} = I_0 S_{hJ} J_{hT} \, , \tag{14}$$

where

$$J_{hT} = \frac{\gamma}{D\Delta\mu} \sqrt{1+W^2} \exp\left(-\mu D/\gamma\right) [(1 - \frac{1}{2(1+W^2)}) \sinh\left(\frac{D\Delta\mu}{\gamma\sqrt{1+W^2}}\right)$$

$$- \frac{W}{\sqrt{1+W^2}} (\cosh\left(\frac{D\Delta\mu}{\gamma\sqrt{1+W^2}}\right) - 1)] \tag{15}$$

and

$$I_{hR} = I_0 S_h J_{hR} \, , \tag{16}$$
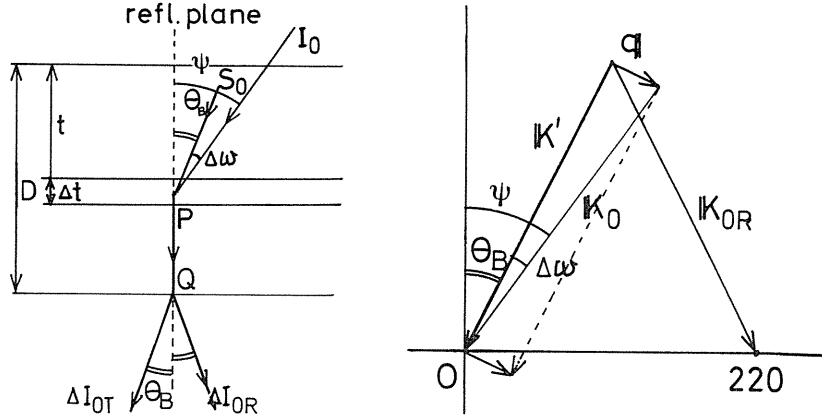
Fig. 19. (a) Ray paths related to diffraction of TDS near the 000 reciprocal lattice point.
(b) Wave vectors in the reciprocal space.

where

$$J_{hR} = \frac{\gamma}{2D\Delta\mu\sqrt{1 + W^2}} \exp\left(-\frac{\mu D}{\gamma}\right) \sinh\left(\frac{D\Delta\mu}{\gamma\sqrt{1 + W^2}}\right).$$ (17)

Figure 19(a) shows that the intensity I_{0R} is to be estimated in the intensity evaluation of the excess line across the thermal diffuse spot near the h reciprocal lattice point. By using the intensity S_0 of the TDS near the origin of the reciprocal space, which is incident on the h reflecting net plane at angle θ_B, we have

$$I_{0R} = I_0 S_0 J_{hR}$$ (18)

where

$$b_0 = K' - K_0 = q.$$ (19)

The wave vector K' belongs to the thermally scattered wave propagating close to the incident beam as shown in Fig. 19(b). Finally, we have the intensity formula of the excess line as

$$I = I_{hT} + I_{0R} = \frac{I_0 S_h \gamma}{D \Delta \mu} \sqrt{1 + W^2} \exp\left(-\frac{\mu D}{\gamma}\right) \left[\left(1 - \frac{1}{2(1 + W^2)}\right)\right.$$

$$\times \sinh\left(\frac{D \Delta \mu}{\gamma \sqrt{1 + W^2}}\right) - \frac{W}{\sqrt{1 + W^2}} \left(\cosh\left(\frac{D \Delta \mu}{\gamma \sqrt{1 + W^2}}\right) - 1\right)\right]$$

$$+ \frac{I_0 S_0 \gamma}{2 D \Delta \mu \sqrt{1 + W^2}} \exp\left(-\frac{\mu D}{\gamma}\right) \sinh\left(\frac{D \Delta \mu}{\gamma \sqrt{1 + W^2}}\right). \tag{20}$$

If we put $S_0 = S(q,q)$ and $S_h = S(q_h, q_h)$ in the above equation, eq. (20) agrees with the intensity eq. (5.5) of Kikuchi line given by Okamoto, Ichinokawa and Ohtsuki[29] except some multiplying constants related to speciality of electron diffraction. Kainuma neglected absorption in his theory[7]. If we take the case of negligible absorption by putting $\mu = 0$ and $\Delta\mu = 0$, replacing S_0 and S_h in eq. (20) with S_{hh} and S_{00}, respectively, eq. (20) agrees with the intensity formula eq. (24) of the diffraction pattern given by Kainuma[7] except the band terms. In the present case $S_0 \ll S_h$, since $S_0/S_h = (b_0/b_h G_h)^2 \ll 1$. Therefore, I_{0R} is negligibly small in comparison with I_{hT} for the h = 220 thermal diffuse scattering. The intensity eq. (20) of the excess line near the reciprocal lattice point h can be expressed approximately by I_{hT}.

1.3.3. *Numerical calculation and comparison with experimental result*

Numerical calculation of the intensity profile across the excess line was carried out to compare with the experimental result using eq. (15), eq. (17) and values in Table 1. The specimen crystal thickness 100 μm is thick enough to produce dynamical diffraction in comparison with the extinction distances 7.0 μm and 11 μm for the 220 reflections of the 1.54Å and 1.15Å radiations, respectively. The result of the calculation about the excess line EL is shown in Figs. 20(a)—(c) and Figs. 21(a)—(d). Since the J_{hT} and J_{hR} in these figures are the intensities relative to the TDS intensity $I_0 S_h$, the intensities I_{hT} and I_{hR} of the excess lines EL and ELR are given by the products $I_0 S_h J_{hT}$ and $I_0 S_h J_{hR}$, respectively. The angle $|\theta - \theta_B|$ corresponding to $|W| = 1$ is a few seconds in arc in the present case. In the case $|W| \gg 1$

Table 1. Parameters for the germanium 220 symmetric reflecton in the Laue case.

wavelength	λ (Å)	1.54051	1.15000
extinction distance	τ_o(μm)	7.0	11
kappa zero	κ_o	−0.9589*	−0.9600**
linear abs. coeff.	μ(1/cm)	353	172
anomalous abs. coeff.	$\Delta\mu$(1/cm)	15	8
gamma	γ	0.9228	0.9578

*   obtained by calculation from the values[30] of ϕ_{oi} and ϕ_{hi}.

** obtained by interpolation of the values[30] of ϕ_{oi} and ϕ_{hi} for Cu Kα_1 and MoKα_1.
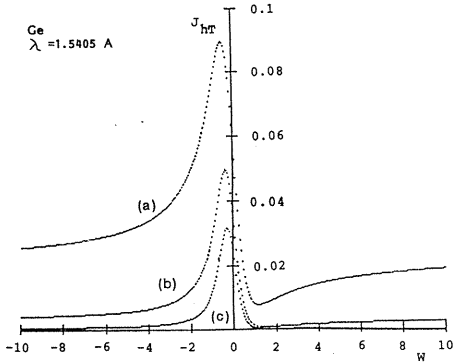
Fig. 20. Calculated profiles of J_{hT} for 1.54Å X-ray and germanium 220. Thickness D, (a) 0.1 mm, (b) 0.15 mm, (c) 0.2 mm.
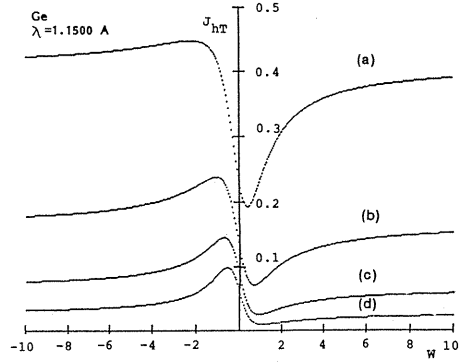
Fig. 21. Calculated profiles of J_{hT} for 1.15Å X-ray and germanium 220. Thickness D, (a) 0.05 mm, (b) 0.1 mm, (c) 0.15 mm, (d) 0.2 mm.

corresponding to $|\theta - \theta_B| \gg 1''$, the J_{hT} and J_{hR} approach to exp $(-\mu D/\gamma)$, the I_{hT} and I_{hR} approach to $I_0 S_h$ exp $(-\mu D/\gamma)$. In the angular region $|\theta - \theta_B| < 1'$, the TDS intensity can be approximated to be constant. The intensity distribution profile of the excess line can be given approximately by J_{hT} and J_{hR} in the narrow angular region near the excess line. The above figures show that the intensity and the profile of the excess line depend on the incident beam. Decrease of the thickness leads to increase of the line intensity, increase of asymmetry of the profile and appearance of the excess-defect line. As the crystal thickness increases, the defect line disappears, the excess line which is approximately symmetric in shape appears and the intensity decreases. Dependence of the line intensity on wavelength of the incident radiation is found, since the absorption coefficient of the specimen depends on the energy of the incident photon. The line due to 1.54Å X-ray and the specimen of thickness 0.1 mm is composed of strongly excess and weakly defect lines as shown in Fig. 20(a). Since the definition of W given by eq. (10) means that positive and negative W correspond to $\theta > \theta_B$ and $\theta < \theta_B$, respectively. Figs. 20 and 21 show that the excess part is on the lower angle side and the defect part on the higher angle side. This means that a white line appears always at the scattering angle higher than that of a black line.

The intensity distribution of the EL line in Figs. 10(a)—(c) corresponds to Fig. 20(a). A sharp and strong black line beside a weak white line can be seen in the corresponding angle side in these figures. Contrast of the black line to the TDS diffuse background is low in Figs. 12 as well as in Fig. 21(b), a black excess line beside a white defect line looks indistinct. The EL and ELR line intensities I_{hT} and I_{hR} depend on product μD as seen in eqs. (14)—(17). The μ value for the 1.54Å X-ray is about twice of the value for the 1.15Å X-ray. This means that the diffraction pattern from the specimen with thickness unity for the 1.15Å X-ray corresponds to the pattern from the specimen with thickness half for the 1.54Å radiation. The diffraction pattern due to the 1.54Å X-ray corresponds to the pattern due to the specimen with thickness double for the 1.15Å X-ray. Thus the calculated result shown in Figs. 20 and 21 agrees well with the experimental result shown in Figs. 10 and 12.

Figures 22 and 23 show the calculated intensity profile of the excess line ELR near the origin of the reciprocal space. The intensity profile of the line depends on the specimen
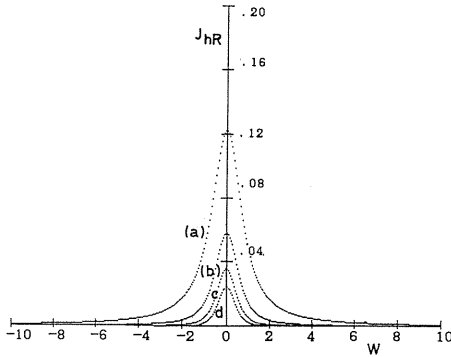
Fig. 22. Calculated profiles of J_{hR} for 1.54Å X-ray and germanium 220. Thickness D, (a) 0.05 mm, (b) 0.1 mm, (c) 0.015 mm, (d) 0.2 mm.
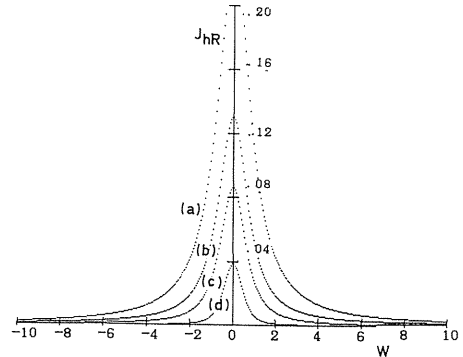
Fig. 23. Calculated profiles of J_{hR} for 1.15Å X-rays. Thickness D, (a) 0.05 mm, (b) 0.1 mm, (c) 0.15 mm, (d) 0.2 mm.

thickness and the incident beam wavelength. The shape of the intensity profile, however, is excess and symmetric always. This result agrees well with the observation as shown in Figs. 13(a) and (b). The pattern similar to Fig. 13 was observed also for the same specimen by using the 1.15Å radiation.

The calculated intensity profile of the TDS diffraction peak was compared with the experimental results in detail[27]. The size of the specimen germanium crystal surfaces was 5 × 5 cm^2. The thicknesses of the specimen A and B were 0.10 mm and 0.25 mm, respectively. The momentum vector of the phonon, needed for calculating S_h, was determined by the scattering angle 2θ and the offset angle $\Delta\omega$. The intensity profile of the diffraction peak calculated by eqs. (14) and (16) should be compared with experiment after performing a convolution to account for the reflection widths of monochromator, collimator, and analyzer. To make the calculation simple, we assume as follows: (1) The incident radiation is of wavelength 1.54Å from an ideally distant point source; we neglect *finite angular and energy widths* scattered dynamically by the monochromator. (2) The resolution function of the collimator and analyzer of grooved silicon crystals, being *tailless* by virtue of five consecutive symmetric 220 Bragg reflections, is approximated simply as

$$C(x) = \left(\begin{array}{ll} 0, & |x| > \Delta\theta_M \\ \\ \text{const}, & |x| < \Delta\theta_M \end{array} \right.$$

where $2\Delta\theta_M$ is the theoretical angular FWHM of the Si 220 Bragg reflection. Here we neglected the energy and spatial divergence of the X-rays passing through the monochromator. The intensity distribution $I_{calc}(x)$ of a diffraction-peak profile was then expressed as double convolutions of $C(x)$ and the theoretical intensity distribution I_{hT} in eq. (14). Then we have

$$I_{calc}(x) = \iint C(x-u) \, I_{hT}(v) \, C(u-v) \mathrm{d}v \, \mathrm{d}u, \tag{21}$$

where x is given by $\Delta\theta$ or $\Delta(2\Delta\theta)$.

Test rocking profiles of the 220 Bragg reflections were found to be in excellent agreement with the profiles calculated by eq. (21). We finally had two important fitting parameters for each specimen: background and reflectivity of the collimator or analyzer. Numerical calculation of the intensity profile of the diffraction peak was carried out to compare with the experimental result by using eq. (21) and the elastic constant values $C_{11} = 12.89 \times 10^{11}$, $C_{12} = 4.88 \times 10^{11}$ and $C_{44} = 6.71 \times 10^{11}$ (dyne/cm^2). Even the thinner specimen A was thick
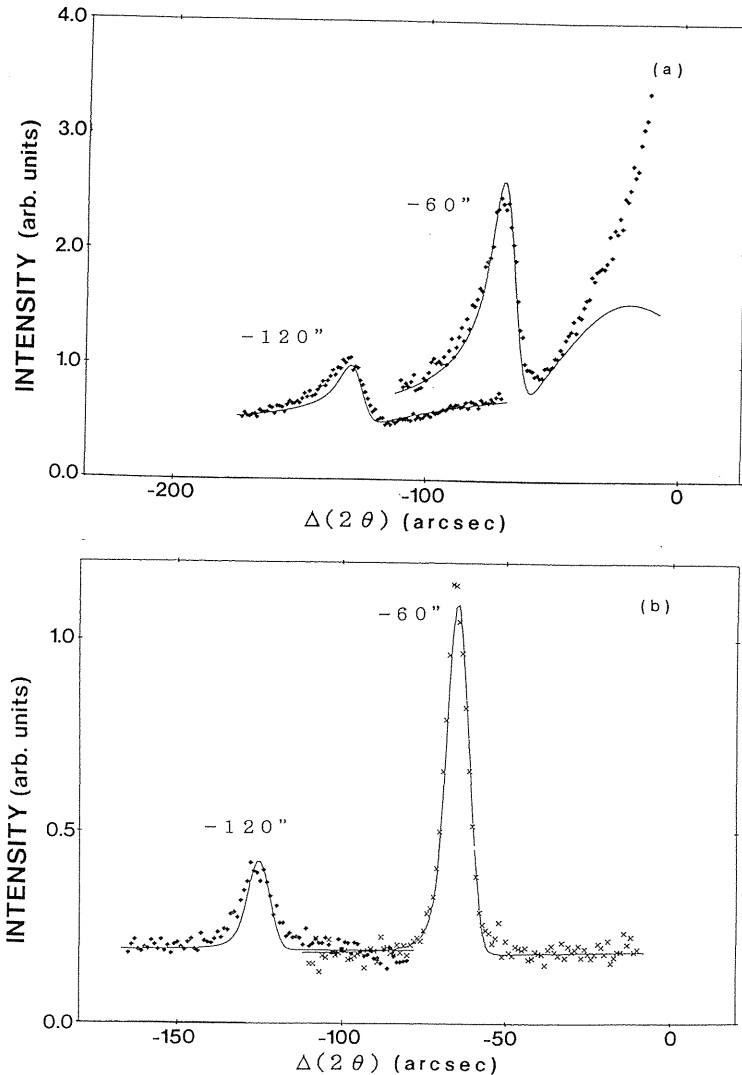
Fig. 24. Observed (marked) and calculated (solid line) intensity profiles across the excess-defect lines in the 220 TDS. (a) specimen A, thickness 0.10 mm, $\Delta\omega = -120''$ and $-60''$. (b) specimen B, thickness 0.25mm, $\Delta\omega = -120''$ and $-60''$.

enough to cause dynamical diffraction and absorption in comparison with the extinction distance 7.2 μm and $\mu D = 3.5$ for the 220 reflection of the 1.54Å X-ray. The fitting calculation was carried out for several offset angles $\Delta \omega$ and specimen thicknesses D, and we added the central angle of the diffraction profile where $\Delta (2\theta) = 0$ as one more fitting parameters. Therefore the absolute value of the peak position is meaningless, and only the relative value is meaningful. Figures 24(a) and (b) show the convoluted theoretical curves (solid line) and experimental curve (marked) for several offset angles of specimens A and B, respectively. All profiles of A and B specimens show good agreement in theory and experiment. They also show that the profile of the diffraction peak mainly depends on the specimen thickness (μD), and its peak intensity depends on the offset angle. Decrease of the specimen thickness leads to increase of the peak intensity and the base (TDS) intensity. In addition, it causes a more asymmetric profile which appears as the excess-defect line. In accordance with increase of the thickness, the diffraction peak becomes more symmetric since it is formed by a part of the TDS X-rays anomalously transmitted with little absorption. The diffraction peaks have following characteristics in addition to the previous summary in section 1.2.2.

(1)   The intensity profile of the diffraction peak varies from excess-defect to excess as the specimen thickness increases. The thickness dependence in the calculated intensity profile explains the experimental result.

(2)   The intensity profile of the diffraction peak of the thinner specimen A is asymmetric with a excess-defect line. The defect part in the excess-defect intensity profile appears at a scattering angle slightly higher than the excess part, which is independent[27] of the sign of the offset angle $\Delta \omega$.

1.4.   Summary, Conclusion and Discussion

Diffraction lines across TDS spots from mosaic crystals were observed by X-ray film photograph and densitometry in the Laue case as well as Bragg case. Good agreement between the expermental results and the calculation of the line intensity distribution across the line was obtained. It is concluded that the origin of the diffraction line from the mosaic crystal is attributed to the secondary extinction effect for the diffraction of TDS.

Diffraction lines across TDS spots and the incident beam spot from nearly perfect crystals were observed by photographic method as well as triple-crystal diffractometry by means of monochromatized synchrotron radiation. The diffractometry measurement was completely in agreement with photographic observation.

Agreement between the experiment and the calculation on the basis of the dynamical diffraction theory leads to the conclusion that the excess lines EL and ELR observed can be explained well as the anomalous transmission and the Bragg reflection of the thermally scattered wave. The crystal orientation dependence and the wavelength dependence of the excess line were observed for the both specimens of germanium and silicon crystals. The intensity of the excess line of TDS depends on the crystal orientation to the incident beam, since the intensity of TDS depends on the propagation direction of the incident X-ray and is inversely proportional to the square of the wave vector q as given in eq. (4). While intensities of Kossel lines caused by fluorescent X-ray and Compton scattering do not depend on the direction of the incident X-ray so much as that caused by TDS, since the intensities of fluorescent X-ray and Compton scattering do not depend on the scattering angle so much as that of TDS.

The intensity formula eq. (24) given by Kainuma[7] for the diffraction pattern caused by the Bragg reflection of TDS contains a band term S_{0h} or S (q, q_h). The intensity formula

eq. (15), however, does not contain the band term. This is due to the fact that the present paper deals with intensity and dose not deal with amplitude of the diffracted wave in the crystal in the derivation of the excess line intensity. This approximation is permitted, since the experimental condition of the present paper is independent of the band. The intensity ratio between those of the band and the excess line is proportional approximately to $S\,(q,q_h)/S$ $(q_h,q_h) = b_0\,G_0\,/\,b_h\,G_h$, which is much smaller than unity in the present case. The band term, however, is to be taken into consideration in the general case.

The theory for nearly perfect crystal is confined to the Laue case so far. The present authors are preparing to report the study about the Bragg case.

References

 1) W. Kossel, V. Loeck and H. Voges: Zeit.f. Physik, **94** (1935) 139.
 2) M. von. Laue: Ann. der Physik, **23** (1935) 705.
 3) Y. Kainuma: Acta Cryst. **8** (1955) 247.
 4) S. Takagi: J. Phys. Soc. Jpn. **13** (1958) 278, 287.
 5) N. Norman: Acta Cryst. **11** (1958) 1.
 6) H. J. Grenville-Wells: Nature **168** (1951) 291.
 7) Y. Kainuma:J. Phys. Soc. Jpn. **16** (1961) 228.
 8) Y. Kainuma: private communication.
 9) T. Seto and T. Hayashida: Meeting of the Physical Society of Japan. 1961.
10) Y. Kashiwase, Y. Kainuma and M. Minoura: J. Phys. Soc. Jpn. **50** (1981) 2793.
11) Y. Kashiwase, Y. Kainuma and M. Minoura: Acta Cryst. **A38** (1982) 390.
12) Y. Kashiwase, Y. Kainuma and M. Minoura: Jpn. J. Appl. Phys. **21** (1982) L34.
13) Y. Kashiwase, M. Mori, M. Kogiso, Y. Oya, M. Minoura, S. Sasaki and T. Ishikawa: *Photon Factory Activity Report* (National Laboratory for Hight Energy Physics, KEK, 1987) p.166.
14) V. A. Bushuev, A. V. Laushkin, R. N. Kuzmin and N. N. Lovanov: Sov. Phys. JETP Lett. **34** (1981) 236.
15) V. A. Bushuev, A. V. Laushkin, R. N. Kuzmin and N. N. Lovanov: Sov.-Solid State **25** (2) (1983) 228.
16) Y. Oya: Thesis of Master's degree, Nagoya Univ. School of Engin. Dept. of Appl. Phys., 1986.
17) Y. Oya and Y. Kashiwase: J. Phys. Soc. Jpn. **57** (1988) 2026.
18) Y. Kashiwase and Y. Kainuma: J. Phys. Soc. Jpn. **51** (1982) 2379.
19) Y. Kashiwase and Y. Kainuma: J. Phys. Soc. Jpn. **53** (1984) 3438.
20) G. Borrmann: Z.f. Phys. **127** (1950) 297.
    G. Borrmann, G. Hildebrandt, and G. Wagner: Z.f. Phys. **142** (1955) 406.
21) M. Kogiso, Y. Kashiwase, M. Mori, M. Minoura, K. Ushida and S. Sasaki: Reported at Annual Meeting of the physical society of Japan, March 31, 1990. To be published.
22) Y. Kashiwase, M. Mori, M. Kogiso, M. Minoura, S. Sasaki and T. Ishikawa: J. Phys. Soc. Jpn. **55** (1986) 4172.
23) Y. Kashiwase, M. Mori, M. Kogiso, M. Minoura and S. Sasaki: J. Phys. Soc. Jpn. **57** (1988) 524.
24) K. Ushida: Thesis of Master's degree, Nagoya Univ. School of Engin. Dept. of Appl. Phys., 1988.
25) Y. Amemiya, T. Matsushita, A. Nakagawa, Y. Satow, J. Miyahara: Nucl. Instr. and Meth. **A266** (1988) 645.
26) Y. Kashiwase, M. Mori, M. Kogiso, K. Ushida, M. Minoura, T. Ishikawa and S. Sasaki: Phys, Rev. Lett. **62** (1989) 925.
27) M. Mori, Y. Kashiwase, M. Kogiso, K. Ushida, M. Minoura, T. Ishikawa and S. Sasaki: Phys, Rev. **45B** (1992) 9583.
28) M. Mori, Y. Kashiwase, M. Kogiso and S. Sasaki: Acta Cryst. **46** (1990) 923.
29) K. Okamoto, T. Ichinokawa and Y. Ohtsuki: J. Phys. Soc. Jpn. **30** (1971) 1690.

30) Z. G. Pinsker: *Dynamical Scattering of X-rays in Crystals*, Springer Series in Solid-State Science (Springer-Verlag, Berlin, Heiderberg, New York, 1978).

II. Dynamical Diffraction Effect on X-Ray Inelastic Scattering

2.1. Introduction

When X-rays are diffracted in a nearly perfect crystal, two types of standing wave fields are produced. One of them has its nodal planes on the diffracting atomic planes and the other between the adjacent atomic planes. Under these conditions, intensity anomalies of inelastic scatterings are caused. Batterman[1] first observed an asymmetric dip in the intensity curve of fluorescent X-rays emitted from a germanium crystal in the Bragg-case diffraction.

The intensity anomalies of thermal diffuse scattering (TDS) and Compton scattering have also been studied in the Bragg case[2-5]. Intensity anomalies of fluorescent X-rays in germanium crystals in the Laue geometry were studied by Annaka[6,7], who observed an intensity decrease and increase from the exit surface of thin and thick crystals, respectively. Comparison between the experimental results and theory, however, was qualitative. Bushuev and Lyubimov[8] also investigated the intensity increase and decrease in the inelastic background including TDS, Compton scattering and fluorescent X-rays accompanying the Laue case 220 reflection in a perfect silicon crystal. The dynamical diffraction effect on fluorescent X-rays from impurity germanium atoms in a silicon crystal was investigated by Kazimirov et al.[9]. The yield of photoelectrons and Auger electrons emitted from single crystals shows anomalous change when incident X-rays satisfy the diffraction condition, since the amount of electron emission is proportional to the intensity of X-ray wave fields formed on the atomic plane. The variations in the yield of K- and L-photoelectrons and KLL Auger electrons emitted from a silicon single crystal under the symmetric[10] and asymmetric[11] 220 diffraction conditions of CuKα radiation were observed by Kikuta and Takahashi.

Diffraction effects on TDS from thick absorbing crystals in the Laue geometry have not been studied in detail. This chapter deals with this subject as well as with its relation to the previously reported dynamical diffraction of TDS[12,13].

Inelastic X-ray background generally may include fluorescent X-rays, and TDS as well as Compton scattering. Experimental separation of TDS and Compton scattering is necessary but difficult problem. The problem of the correction is not important for the study of fluorescent X-rays, when the intensity of fluorescent X-rays is much stronger than those of TDS and Compton scattering. The problem is further simplified by the fact that emission of fluorescent X-rays can be assumed to be isotropic. The dynamical diffraction effect on fluorescent X-rays is a reciprocal process of the Borrmann effect on Kossel lines. The problem in a thick absorbing germanium crystal, where fluorescent X-rays are much stronger than TDS and Compton scattering, has not been thoroughly investigated yet. This chapter also reports the dynamical diffraction effect of incident X-rays on fluorescent X-ray emission in thick absorbing germanium crystals in the simplest experimental conditions.

2.2. The Effect on Thermal Diffuse Scattering[13]

The intensity measurement was performed at room temperature with the vertically dispersive high-precision goniometer system[14,15] installed on PF, BL-15C. Fig. 1 illustrates the system. Synchrotron radiation of wavelength 1.54Å, monochromatized with the symmetric silicon 111 reflection M, and five successive 220 reflections in a channel-cut silicon collimator[16,17] C, was incident on the (100) surface of a nearly perfect germanium crystal S, of size 10×10 mm^2. Two samples with thicknesses 0.20 mm and 0.30 mm (absorption coefficient μ times thicknesses D are 5.3 and 7.95, respectively) set at the 022 Bragg position in the Laue geometry were studied. The cross section of the beam was about 1×1 mm^2 on the specimen. The beam divergence was about 10 arc sec in the horizontal plane and 4 arc sec in the vertical plane. The intensities of the transmitted beam, the 022 refracted beam and the inelastic scattering were measured simultaneously with scintillation detectors D1, D2 and D3, respectively. The incident beam was monitored by an ionization chamber IC, during the measurement. The distances between the collimator and the specimen and between the specimen and the counters were about 70 cm and 15 cm, respectively. The window of the detector D3 was about 15 mm in diameter. The intensity measurement was made by rotating the specimen crystal stepwise across the 022 Bragg position with the counters fixed. The observed intensities were normalized by the monitor counts.

Inelastic intensities were measured at point P1 on the Ewald sphere close to the 133 reciprocal-lattice point in the plane including the [100] and [011] axes in Fig. 2. The open circles in Figs. 3(a), (b) and (c) show the experimental rocking curve of the transmitted beam and the measured intensity variations of inelastic scatterings at points P1 and P2, respectively, in Fig. 2 for the thick specimen. The intensities are plotted against $\Delta\theta = \theta - \theta_B$, the angular deviation of the crystal orientation from the Bragg angle θ_B. The open circles in Figs. 4(a), (b) and (c) show the measured intensities for the thin specimen, corresponding to those in Figs. 3(a), (b) and (c), respectively. Actual counts at the inelastic peaks were about (2 −
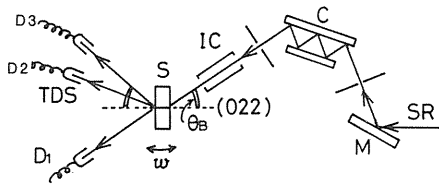

Fig. 1. Experimental arrangement in a vertical plane. SR, synchrotron radiation; M, silicon (111) monochromator; C, grooved silicon crystal with (220) surfaces; IC, monitor; S, specimen; D1, D2 and D3, detectors.
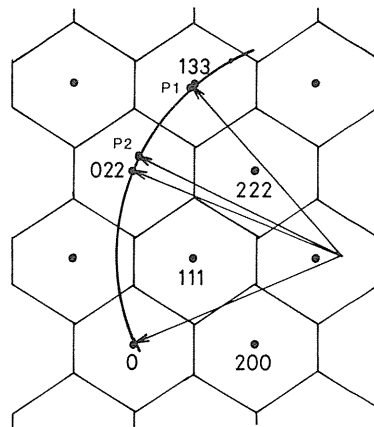

Fig. 2. (a) Geometry of X-ray and specimen crystal orientation, (b) Ewald sphere, observed points P1 and P2 in the reciprocal lattice of specimen crystal.
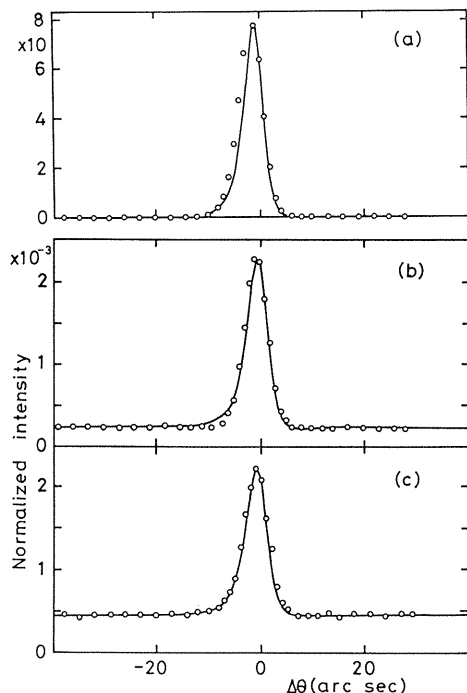
Fig. 3. Observed (open circles) and calculated (solid line) intensity curves. (a) transmitted beam; (b) inelastic scatterings at P2 near the 022 reciprocal lattice point (r.l.p); (c) inelastic scattering at P1 close to the 133 (r.l.p), the specimen thickness 0.30 mm.
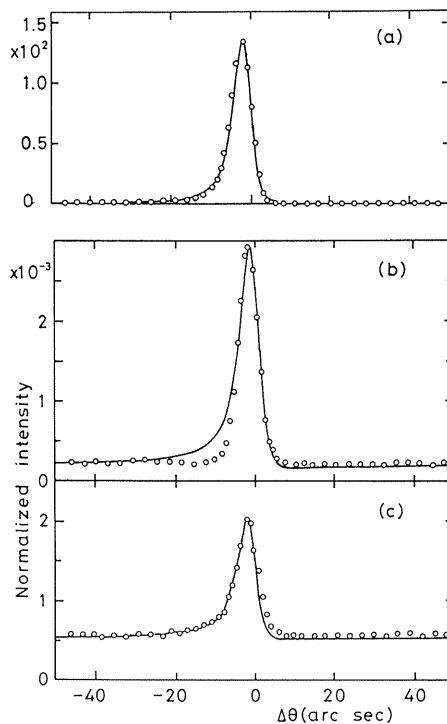
Fig. 4. Open circles and solid lines for the specimen of thickness 0.20 mm in (a), (b) and (c) correspond to those in Figs. 3(a), (b) and (c), respectively.

3) $\times$ 10^3 per 50 s. A good agreement between the experimental rocking curves and the calculations in Figs. 3(a) and 4(a) show that the specimen crystals are sufficiently perfect for the anomalous transmission to occur. As for the inelastic intensity, the following features are noted. (1) The inelastic scattering curve shows an asymmetric peak profile. (2) The peak width and the peak position are close to those for the transmitted beam. (3) The profile, width and height of the inelastic peak depend on specimen thickness. The thin specimen shows a more pronounced asymmetric profile than the thick one. The main part of the observed inelastic intensities is TDS, since the observation points are close to the reciprocal lattice points.

The experimental results are compared with calculations based on the dynamical theory. Propagation of X-rays in a parallel plate crystal of thickness D is illustrated schematically in Fig. 5(a). Monochromatic plane-wave X-rays with intensity I_0 are incident on the (022) planes normal to the surface at the glancing angle $\theta = \theta_B + \Delta\theta$. The X-rays are linearly polarized with the electric field vector perpendicular to the diffraction plane. When the Bragg reflection is strongly excited in a narrow angular region $2\Delta\theta_B$ centered nearly at $\Delta\theta = 0$, the transmitted and reflected waves interact to form two wave fields which are strongly or
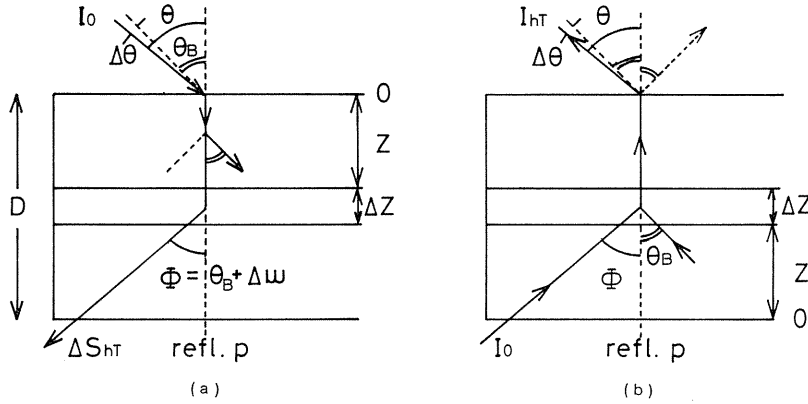
Fig. 5. Diffraction and inelastic scattering process. (a) Present diffraction effect on inelastic scattering.
(b) Dynamical diffraction of inelastically scatterd waves.

weakly absorbed according to whether they have antinodes or nodes on the reflection planes. The transmitted beam produces inelastic scattering with intensity $\Delta S_h = S_h \, \Delta z/D$ from layer Δz at depth z, which proceeds to an observation point near the h reciprocal-lattice point in the direction $\Phi = \theta_B + \Delta\theta \gg \Delta\theta_B$. Here the factor S_h is the intensity of kinematical inelastic scatterings (including TDS and Compton scattering) for unit incidence intensity. The scattered waves attenuate owing to the ordinary absorption before reaching the exit surface. The inelastic intensity is given as

$$\Delta S_{hT} = I_0 \, G_T(z) S_h \, (\Delta z/D) \, \exp\{-\mu(D-z)/\gamma\}\,, \tag{1}$$

with

$$G_T(z) = \frac{1}{2} \left[\begin{array}{l} \dfrac{1}{2}\,(1 - \dfrac{W}{\sqrt{1+W^2}})^2 \, \exp(-\dfrac{\mu z}{\gamma}\,(1 - \dfrac{\kappa_0}{\sqrt{1+W^2}})) \\[3mm] + \dfrac{1}{2}\,(1 + \dfrac{W}{\sqrt{1+W^2}})^2 \, \exp(-\dfrac{\mu z}{\gamma}\,(1 + \dfrac{\kappa_0}{\sqrt{1+W^2}})) \end{array} \right]\,, \tag{8}$$

Definition of γ, κ_0 and W are already given in section 1.3.2. Comparing Fig. 5(a) with Fig. 5(b), which illustrates the dynamical diffraction of TDS[13] by layer Δz, we can see that the diffraction and scattering processes in Figs. 5(a) and 5(b) are just reciprocal. The intensity of inelastic scattering from layer Δz in Fig. 4(b) is given by

$$\Delta I_{hT} = I_0 \, \exp(-\mu z/\gamma) \, S_h(\Delta z/D) \, G_T(D-z)\,. \tag{3}$$

Integrations of eqs. (1) and (3) lead to the same result:

$$S_{hT} = I_0 S_h J_{hT} , \tag{4}$$

with

$$J_{hT} = \frac{\gamma}{D \Delta \mu} \sqrt{1 + W^2} \exp\left(-\mu D/\gamma\right) \left[\left(1 - \frac{1}{2(1 + W^2)}\right) \sinh\left(\frac{D \Delta \mu}{\gamma \sqrt{1 + W^2}}\right)\right.$$

$$\left. - \frac{W}{\sqrt{1 + W^2}} \left(\cosh\left(\frac{D \Delta \mu}{\gamma \sqrt{1 + W^2}}\right) - 1\right)\right] \tag{5}$$

The profile of the inelastic peak is determined by eq. (5), since J_{hT} is a sharp function of $\Delta\theta$ in a very narrow angular region, while S_h is a slowly varying function of the scattering vector. The solid lines in Figs. 3(b) and (c) and in Figs. 4(b) and (c) show the J_{hT} calculated for the present experimental conditions by using $\mu = 352\,\text{cm}^{-1}$ and $\Delta\mu = 326\,\text{cm}^{-1}$ in eq. (5) and normalized at the top of the experimental peak. The asymmetric reflection correction required for the theoretical calculation of J_{hT} at the point P2 is small and neglected in Figs. 3(c) and 4(c). The solid lines show a good agreement with observed inelastic peak profiles except in Fig. 4(b). A small disagreement between the observed and calculated peak widths is ascribable to the fact that the calculated curve is not convoluted with the diffraction profile of the monochromator. The present theoretical calculation neglects inelastic scattering of the 022 Bragg diffracted beam.

2.3. The Effect on Fluorescent X-Rays[18]

Figure 6 illustrates the experimental arrangement of X-ray diffractometry. Radiation from a X-ray tube operated at 40 kV and 25 mA was monochromatized by the silicon 111 symmetric reflection and collimated by the triple 220 symmetric reflections in a channel-cut silicon crystal. The radiation of wavelength 0.7093 Å was incident on the (001) surface of nearly perfect germanium crystals in the Laue geometry at room temperature. The angular
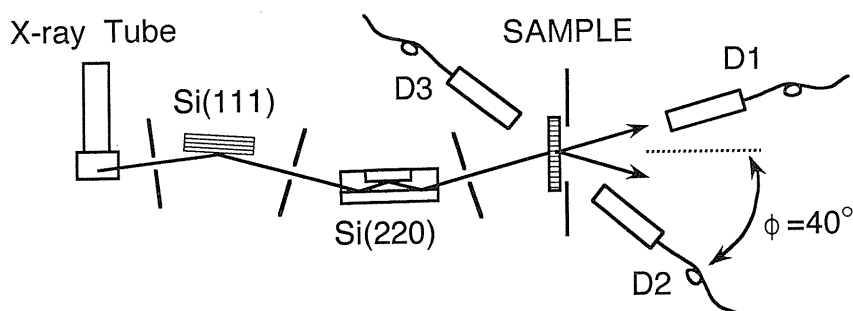

Fig. 6. Experimental arrangement of triple-crystal spectrometer. Ray-paths are in a horizontal plane. D1, D2 and D3 are scintillation detectors.

divergences of incident beam were 2.2″ and 3.5′ in the horizontal and vertical planes, respectively. The specimens with thickness 0.30 mm and 0.52 mm (absorption coefficient times thickness μD is 9.57 and 16.0, respectively) were set near the 220 Bragg position. The measurement of the intensity of the transmitted radiation and of the fluorescent X-rays were performed simultaneously using the step-scanning method with the scintillation counters D1, D2 and D3 and pulse height analyzers in a computer-controlled system. Noise from the counters amounted to few counts per minute. The counters were fixed, and only the specimen was rotated around the [110] axis by a tangential screw with an accuracy of 0.1 arcsec. The distances from the specimen to the counters D1, D2 and D3 were 5 cm, 5 cm and 4 cm, respectively. The window diameter of D1 was 5 mm, and that of D2 and D3 was about 25 mm. Intensities of fluorescent X-rays were measured at 40 degrees from the normal of the exit and incident surfaces of the specimen in the horizontal diffraction plane. A pure germanium solid-state detector which has an energy resolution of about 250 eV was used to check TDS and Compton scattering of which the intensity is few percent of Ge $K\alpha_1$ fluorescent X-rays.

The open circles in Figs. 7(a), (b) and (c) show the experimental rocking curves of the transmitted beam, and the intensity variations of fluorescent X-rays measured by D2 and D3, respectively, for the thin specimen. Counts per 200 seconds for the curves in Figs. 7(a) and (b), and per 100 seconds for the curve in Fig. 7(c) are plotted against $\Delta\theta = \theta - \theta_B$. Solid curves are obtained by the theoretical calculation described below. The open circles in Figs. 8(a), (b) and (c) show the measured rocking curves of the transmitted beam and the intensity variations of fluorescent X-rays measured by D2 and D3 for the thick specimen. Counts per 100 seconds for the curve in Fig. 8(b) and per 10 seconds for the curves in Figs. 8(a) and (c) are plotted against $\Delta\theta$. A satisfactory agreement between the experimental and calculated rocking curves in Fig. 7(a) and Fig. 8(a) shows that the geometry of the specimen crystals allows anomalous transmission to occur. The theoretical curves are corrected for the incident beam divergence. The specific features of the intensity curves of fluorescent X-rays are summarized as follows. (1) The fluorescent curves measured by D2 and by D3 show slightly asymmetric peak profiles and asymmetric dips, respectively. (2) The fluorescence peak and dip are wider than the transmitted beam. (3) The profile, width, peak height and dip depth of the fluorescent intensity curve, and the background level are dependent on specimen thickness.

The solid curves in Figs. 7(b) and 8(b) were obtained using Annaka's formula[3],

$$I_F = \int_0^D \left\{ \frac{\partial}{\partial z}(I_T/I_0) + \frac{\partial}{\partial z}(I_H/I_0) \right\} \exp\left\{ -\frac{\mu}{\gamma}(D-z) \right\} dz \,, \tag{6}$$

where I_0, I_T and I_H are the incident beam intensity, and the transmitted and reflected intensities of the dynamical diffraction given by

$$I_T/I_0 = \frac{1}{4}\left[\begin{array}{l} (1 - \frac{W}{\sqrt{1+W^2}})^2 \exp(-\frac{\mu z}{\gamma}(1 - \frac{\kappa_0}{\sqrt{1+W^2}})) \\[2mm] + (1 + \frac{W}{\sqrt{1+W^2}})^2 \exp(-\frac{\mu z}{\gamma}(1 + \frac{\kappa_0}{\sqrt{1+W^2}})) \end{array} \right], \tag{7}$$
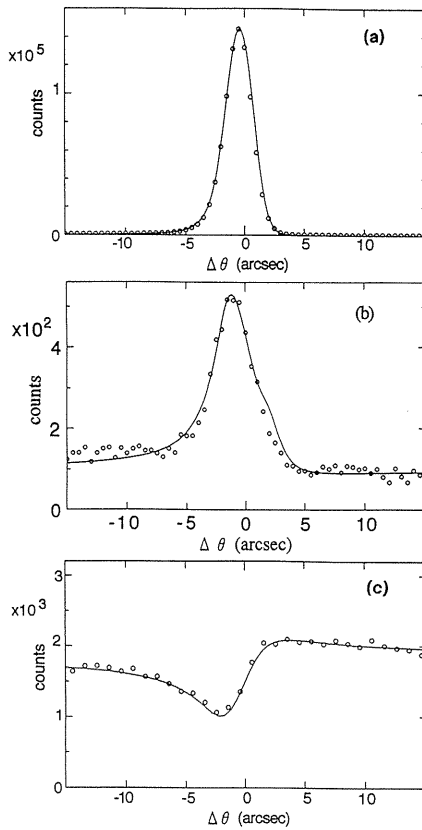
and

Fig. 7. Observed (open circles) and calculated (solid curve) intensities. (a) the transmitted X-ray beam detected by D1; (b) and (c), fluorescent X-rays detected by D2 and D3, respectively. Specimen thickness 0.30 mm. Measurement times for observed points are 200 s in (a) and (b), and 100 s in (c).
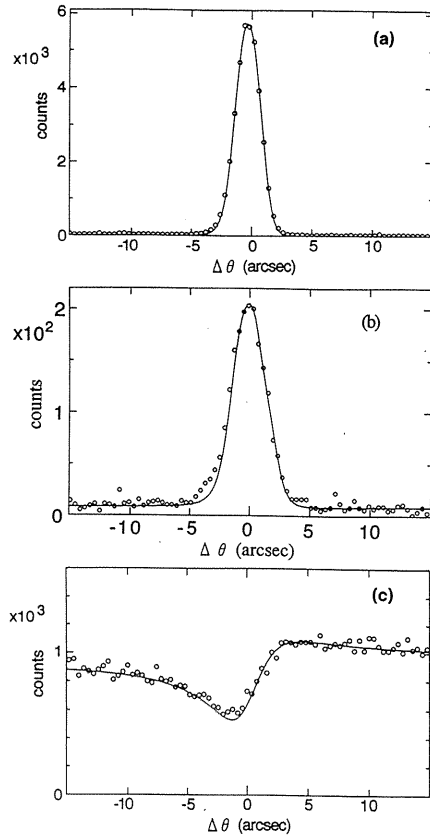
Fig. 8. Open circles observed and solid curves calculated. Specimen thickness 0.52 mm. However, measurement times are 10 s in (a) and (c), and 100 s in (b).

$$I_{\mathrm{H}}/I_0 = \frac{1}{2}\,\frac{1}{(1+W^2)}\,\exp\left(-\frac{\mu z}{\gamma}\right)\cosh\left(\frac{1}{\gamma}\,\frac{Kz\Delta\mu}{\sqrt{1+W^2}}\right). \qquad (8)$$

Here, K equals 1 and cos $(2\theta_{\mathrm{B}})$ for the σ and π states of polarization. Eq. (1) is derived on the basis that fluorescent X-ray emission is isotropic, and TDS and Compton scattering are negligible. In the intensity calculation of eq. (6), the incident beam is assumed to be σ polarized, since the polarization dependence on intensity curves is negligible. The components of Ge $K\alpha_1$, $K\alpha_2$, $K\beta_1$, $K\beta_2$, having intensity ratios 1, 0.50, 0.14 and 0.07 as well as absorption coefficients were taken into consideration. For the parameters of diffraction of the

incident beam, $319\,\mathrm{cm}^{-1}$ and $307\,\mathrm{cm}^{-1}$ were used as values of normal and anomalous absorption coefficients μ and $\Delta\mu$, respectively, and 4.595×10^{-6} as the real part of electric susceptibility for the Ge 220 reflection. The solid curves in Figs. 7(c) and 8(c) were obtained by using the formula

$$I_{\mathrm{F}} = \int_0^D \left\{ \frac{\partial}{\partial z} \left(I_{\mathrm{T}} / I_0 \right) + \frac{\partial}{\partial z} \left(I_{\mathrm{H}} / I_0 \right) \right\} \exp\left(-\frac{\mu z}{\gamma} \right) \mathrm{d}z \,, \tag{9}$$

Comparison between the experimental curves and the calculated solid curves in Figs. 7(b) and 8(c) show that the solid curves agree well with the experimental results.

2.4. Summary, Conclusion and Discussion

In conclusion, we have observed an intensity increase of inelastic X-ray scattering near Bragg points from thick absorbing crystals in the Laue-case diffraction. The main features are explained by the TDS from atomic layers near the exit surface excited by the anomalously transmitting waves. Inelastic scatterings from atomic layers near the entrance surface are almost absorbed and not detected. We can explain the result as a reciprocal process of the dynamical diffraction of inelastic scattering[12,13].

It is ascertained also that Annaka's formula can explain well the dynamical diffraction effect on fluorescent X-ray emission. It is expected that the experimental results can also be explained by Takahashi and Kikuta's formula (10) in ref. 11.

References

1) W. Batterman: Phys. Rev. **133** (1964) A759.
2) S. Annaka, S. Kikuta and K. Kohra: Phys. Soc. Jpn. **21** (1966) 1559.
3) S. Annaka: J. Phys. Soc. Jpn. **24** (1968) 1332.
4) V. A. Bushuev, A. G. Lyubimov and R. N. Kuz'min: Sov. Tech. Phys. Lett. **12** (1986) 60.
5) A. M. Afanas'ev, R. M. Imanov, E. Kh. Mukhamedzhanov and Li Kong Kui: Sov. Phys.-Dokl. **31** (1986) 492.
6) S. Annaka: J. Phys. Soc. Jpn. **23** (1967) 372.
7) S. Annaka: J. Phys. Soc. Jpn. **30** (1971) 1214.
8) V. A. Bushuev and A. G. Lyubimov: Sov. Tech. Phys. Lett. **13** (6) (1987) 309.
9) A. Y. Kazimirov, M. V. Kovalchuk and V. G. Kohn: Acta Crystallogr. **A46** (1990) 649.
10) S. Kikuta and T. Takahashi: Jpn. J. Appl. Phys. **17** (1978) Suppl. 17-2, p.271.
11) T. Takahashi and S. Kikuta: J. Phys. Soc. Jpn. **46** (1979) 1608.
12) Y. Kashiwase, M. Mori, M. Kogiso, M. Minoura and S. Sasaki: J. Phys. Soc. Jpn. **57** (1988) 524.
13) Y. Kashiwase, M. Kogiso, M. Mori, M. Minoura, T. Ishikawa and X. W. Zhang: J. Phys. Soc. Jpn. **60** (1991) 2554.
14) Y. Kashiwase, M. Mori, M. Kogiso, K. Ushida, M. Minoura, T. Ishikawa and S. Sasaki: Phys. Rev. Lett. **62** (1989) 925.
15) Y. Ishikawa, J. Matsui and T. Kitano: Nucl. Instrum. & Methods **A246** (1986) 613.
16) U. Bonse and M. Hart: Appl. Phys. Lett. **7** (1965) 238.
17) T. Matsushita, T. Ishikawa and K. Kohra: J. Appl. Crystallogr. **17** (1984) 257.
18) K. Kaneko, Y. Kashiwase, M. Kogiso, M. Mori and M. Minoura: J. Phys. Soc. Jpn. **62** (1993) 455.

III. Diffraction of Phonon-Scattered Mössbauer Gamma-Ray

3.1. Introduction

Mössbauer γ-ray diffraction has been successfully used to separate intensity of inelastic scattering under Bragg peaks[1,2] with an energy resolution of a few 10^{-8} eV by using the nuclear resonance absorption of γ-ray emitted recoiless from a Mössbauer source. Dips of the inelastic intensity profile at the Bragg angle have been observed by O'Connor and Butt[1] on the 200 reflection from a LiF crystal, and by Zasimov et al.[3] on the 002 reflection from a pyrolytic graphite crystal. The formers explained this result by extinction effects. The latters explained it by mosaic block size characterizing a minimum wave number q_{min} leading to missing inelastic scattering possibilities of lower energies than $\omega(q_{min})$. Müllner et al.[4], however, have not observed the dip in the inelastic intensity profile at any of the four $00h$ reflections from 002 to 008 of a pyrolytic graphite (PG) crystal. Although, their angular divergence of scattered radiations subtended by their detector window was as large as a few degrees.

The present authors found dips in inelastic peaks near Bragg reflections from LiF[5], KCl[6] and PG crystal[7] using Mössbauer 14.4 keV γ-ray and a linear position sensitive detector[5] which has angular resolution of scattered rays as 10 minutes. The dip can be explained by secondary extinction effect[8] as well as diffraction effect[9] caused by thermal diffuse scattering (TDS) reflected again by the net planes in the same crystal. The theory on the diffraction pattern caused by the TDS X-rays has been given by Kainuma[9]. The patterns have been observed in the TDS near the 002 reflection by crystals of urea nitrate[10] and PG[11] in the diffraction patterns recorded on X-ray films using unfiltered radiation from a copper target as already described in chapter I.

The present chapter clarifies the correspondence between the dip in the inelastic intensity profile within and near the Bragg reflection observed by means of Mössbauer diffraction and the defect line observed in the X-ray film. In this experiment, MoKα radiation was used for the X-ray film method and 14.4 keV γ-rays for the Mössbauer diffraction. The wavelengths of the MoKα X-ray and the 14.4 keV γ-ray, 0.7107Å and 0.8602Å, respectively, are close to each other. A pyrolytic graphite crystal was selected as the specimen.

The aim of this chapter is to add experimental evidences of dips corresponding to the intensity distribution across defect lines observed by photographic method as well as X-ray diffractometry.

3.2. Experimental Method and Result

Figs. 1 and 2 show a photograph of experimental instrument and the illustration of the arrangement, respectively. The 14.4 keV γ-rays from a 10 mCi Mössbauer source of ^{57}Co diffused in a 6 μm thick rhodium foil were incident with a fixed glancing angle θ_0 on the specimen surface. The intensity of scattered radiation was measured through the Mössbauer resonant absorber, lithium ammonium ferrofluorate in a plastic disk of diameter 25 mm and thickness 2 mm, set in front of a position sensitive detector window. The enrichment of ^{57}Fe in the absorber is 95.45% with thickness equal to 2 mg/cm^2 of ^{57}Fe. The detector has a space resolution 0.25 mm in the horizontal diffraction plane. The angular divergence of the incident beam was 3° in the diffraction plane and 5° in the vertical plane. Energy resolution of the detector for the γ-rays was about 3 keV. The distances between the source and a
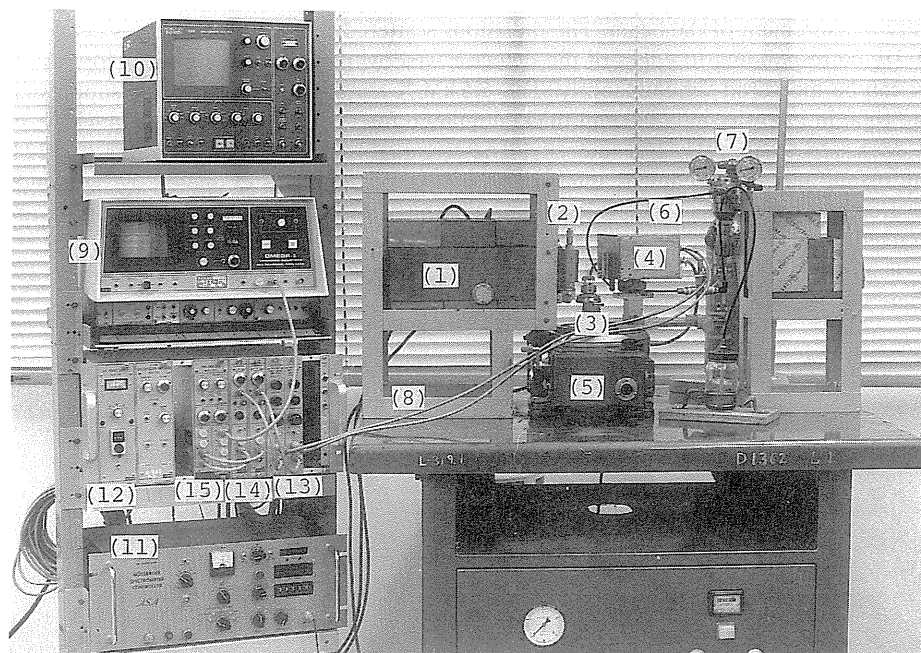
Fig. 1. Instrument of Mössbauer diffraction experiment. (1) lead shield box containing radio-isotope RI at the head of a linear motor driver LM, (2) incident beam slit, (3) goniometer head, (4) position-sensitive detector, (5) goniometer, (6) gas-tube, (7) gas container, (8) cable, (9) multi-channel analyzer, (10)(11) linear-motor controller, (12) high voltage source, (13) shaping amplifier, (14) constant-fraction discriminator, (15) time-amplitude convertor.
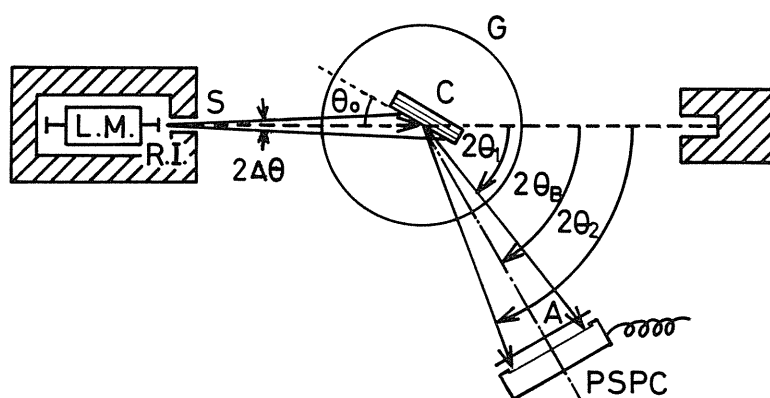

Fig. 2. Arrangement of the experimental devices. RI, Mössbauer source glued to a holder set on the LM; C, crystal; G, goniometer; A, absorber; PSPC, position sensitive proportional detector. Angles $2\theta_1$ and $2\theta_2$ correspond to the edges of the slit before the detector window.

specimen, the specimen and the detector were both 70 mm. The detector window with a lead slit about 10 mm wide and 8 mm high was fixed normal to the reflected beam during an intensity measurement of the beam. The radiations scattered with scattering angles between $2\theta_1$ and $2\theta_2$ corresponding to edges of the detector window or the receiving slit before the window can be measured simultaneously. The 6.5 kV X-ray from the source was suppressed to be 1/1000 in intensity by a 0.3 mm thick aluminum filter, through which the 14.4 keV γ-ray was decreased to about 1/2 in intensity. The remarkably large background due to 122 keV γ-ray mainly was observed. The intensity of the background was evaluated by two kinds of measurement, one with a 2 mm thick aluminium filter and the other without the filter of the diffracted beams.

The intensities I_{el} and I_{in} of the elastic and inelastic scatterings at scattering angle 2θ are obtained by calculation using the formulae[1,2]

$$I_{el}(2\theta) = (I_\infty(2\theta) - I_R(2\theta))/P_0 , \tag{1}$$

with

$$P_0 = (I_\infty(0) - I_R(0))/I_\infty(0), \tag{2}$$

and

$$I_{in}(2\theta) = I_\infty(2\theta) - I_{el}(2\theta) , \tag{3}$$

where $I_\infty(2\theta)$ and $I_R(2\theta)$ are the intensities of the γ-rays scattered at the angle 2θ with the Mössbauer source in motion out of resonance and at rest in resonance, respectively. The absorber efficiency P_0 was measured in the separate experiment using the direct beam from the source by removing the specimen crystal from the beam. The value of P_0 was 0.525 ± 0.013 which was determined using a solid state detector with window slit 1 mm wide and 8 mm high having energy resolution about 200 eV in FWHM (full width at half maximum) for the radiation used. The P_0 value was measured with the position sensitive detector also. The local P_0 value corresponding to the width of position resolution was measured. The average P_0 value was found to be about 5% less than that obtained by the solid state detector. Local variation of P_0, variation of value due to inhomogeneity of absorber thickness, was found to be within about 5%. The effect of the variation of P_0 value on the dip in the inelastic intensity profile was evaluated. There was no remarkable change in the position of intensity minimum and the shape of the dip due to the variation of P_0 value.

3.2.1. *Mössbauer diffraction and X-ray film observations of pyrolytic graphite*[11]

Figures 3 and 4 show the intensity profiles of the elastic and inelastic scattering around the 002 Bragg reflections from a PG specimen obtained by the Mössbauer diffraction experiment. The specimen has a rectangular surface of 10 mm × 10 mm and a thickness of 1 mm. Open and filled circles are the experimental plots for 1/10 times elastic intensities, $I_{el}/10$, and inelastic intensities I_{in}. In the figures, the integrated counts per angular width 15 min are plotted against the scattering angle 2θ. Dips in the inelastic scattering are seen at the position shown by the arrow in the both figures. The difference between the scattering angles corresponding to the intensity maximum of elastic scattering and the intensity minimum in the dip can be seen to be roughly equal to the value of $\Delta\omega = \theta_0 - \theta_B$. Although the θ_0
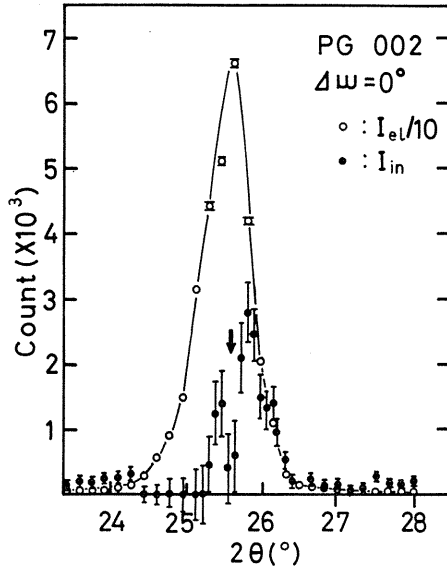
Fig. 3. Intensity profiles of $I_{el}/10$ and I_{in} in the 002 reflection from a PG crystal, $\Delta\omega = 0$. An arrow indicates the position of the intensity minimum in the dip.
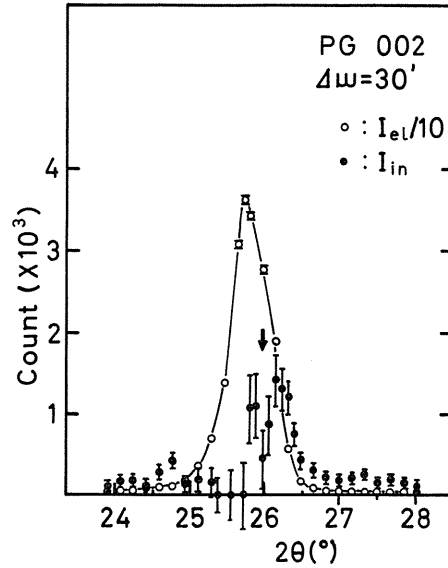
Fig. 4. Intensity profiles of $I_{el}/10$ and I_{in} in the PG 002 reflection, $\Delta\omega = 30'$. An arrow indicates the position of the intensity minimum in the dip.

deviates by $\Delta\omega$ from the Bragg angle, rather weak Bragg reflection is excited and observed due to a large angular divergence of the incident beam.

   In the film observation, unfiltered radiation from a molybdenum target in a sealed-off X-ray tube operated at 30 keV and 15 mA were incident with a glancing angle θ_0 on a flat surface parallel to (001) of the PG plate. The crystal was set on the goniometer head of a Laue camera. The incident beam was collimated using a tube of length 60 mm and an aperture of diameter 0.5 mm. The distance between the source and the crystal was about 130 mm. The camera length between the crystal and the film set normal to the incident beam collimator was about 85 mm. Figs. 5 (a) and (b) show the Laue photographs taken at glancing angles 5.5° and 6.8°, respectively. The Bragg angle θ_B of the 002 reflection is 6.1° for MoKα X-rays. Figs. 6 (a) and (b) illustrate the patterns schematically. Diffuse spots A and A′ are caused by TDS near the 002 and 004 reciprocal lattice points, respectively, by the Kα radiation. Sharp long defect lines D can be seen across the middle of the diffuse spot A and Laue spot C. An excess line E, which is the pair to the defect line, is seen in the diffuse spot due to the incident beam O. The direction of the line E deviates by an angle $\Delta\omega = \theta_0 - \theta_B$ from the direction of the incident beam O. The formation of the diffraction pattern can be explained using Fig. 2 in chapter 1 on the assumption that diffraction of inelastically scattered X-ray is kinematical.
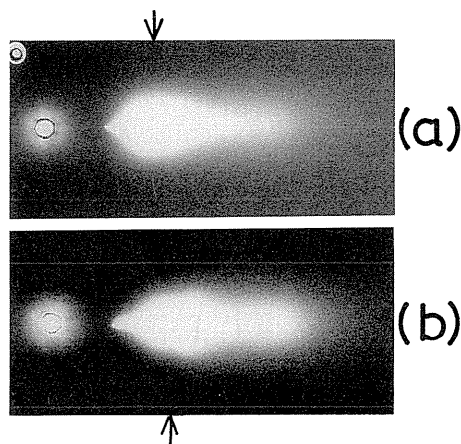
Fig. 5. Laue photograph of the pyrolytic gra-
phite crystal. The sizes of the figures are
the same as those of the original ones.
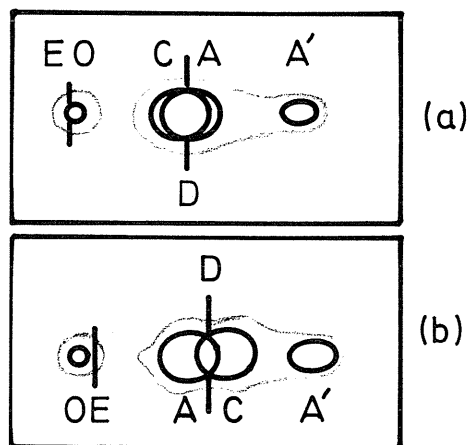Defect lines are indicated by arrows.

Fig. 6. Schematic illustration of the patterns in
Fig. 5.

3.2.2. Mössbauer diffraction of KCl[6]

The radiation from the source was incident with glancing angle θ_0 on the surface cleft parallel to (100) plane of the KCl crystal with 10 mm × 10 mm square area and thickness 5 mm. Fig 7 illustrates the typical result obtained for the 200 Bragg reflection by the KCl crystal. The integrated counts per angular width 20 minutes against 2θ were plotted in the figure. The crystal was set at $\Delta\omega = +30'$. The scattering angle 2θ of the beam corresponding to the maximum of the intensity profile is $2\theta_B$. Filled circle and open circles are the experimental plots for I_∞ and I_R, respectively. The plots I_B in the dotted curve are measured using the aluminium absorber plate of thickness 2 mm before the detector. The background is due to the 122 keV γ-ray.

The intensity profiles of the elastic and inelastic scatterings obtained from the data in the above figures are shown in Fig. 8 with the same scales as given in Fig. 7. The open and filled circles are the experimental plots for the elastic and inelastic scatterings, respectively. Fig. 9 illustrates the intensity profiles of the inelastic scattering as well as that of the elastic scattering within and near the 200 Bragg reflections. In the figure, the integrated counts per angular width 20 minutes are plotted against the scattering angle 2θ. The inelastic scatterings are estimated to be the TDS plus the monotonic background of the Compton scattering. Remarkable dips are seen in every intensity profile of the inelastic scattering. The deviations between the scattering angles corresponding to the intensity maximum of elastic scattering and to the intensity minimum of the dips of inelastic scattering can be seen roughly equal to the value of $\Delta\omega$ from the figures.

The physical explanation of the dips may be given in the same way as that described in the Chapter I. Quantitative comparison between theoretical calculation and the experimental intensity profile of the dips has not been given yet. The wide width of the dip is related to reflection width[8] of mosaicness of the specimen crystal, the divergence of the incident beam and angular resolution of the detector.
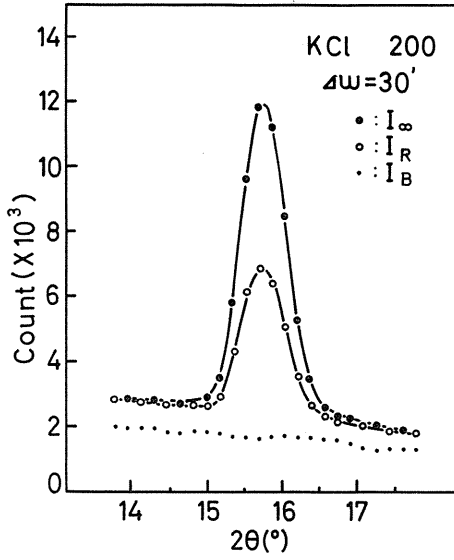
Fig. 7. Intensity profiles of the 200 Bragg reflection from a KCl crystal, $\Delta\omega = 30'$. Experimental plots I_∞ and I_R were measured with the Mössbauer source in motion out of resonance and at rest in resonance, respectively.

Fig. 8. Intensity profiles of the elastic (O) and inelastic scatterings (●), I_{el} and I_{in}, in the KCl 200 Bragg reflection in the case given in Fig. 7.

Fig. 9. Intensity profiles of I_{el} and I_{in} in the KCl 200 Bragg reflection, $\Delta\omega = -26'$.

3.3. Summary, Conclusion and Discussion

The main fact obtained from the present experiment is summarized as follows:

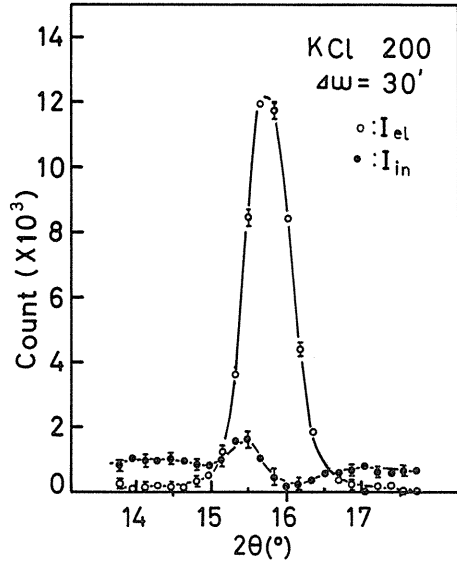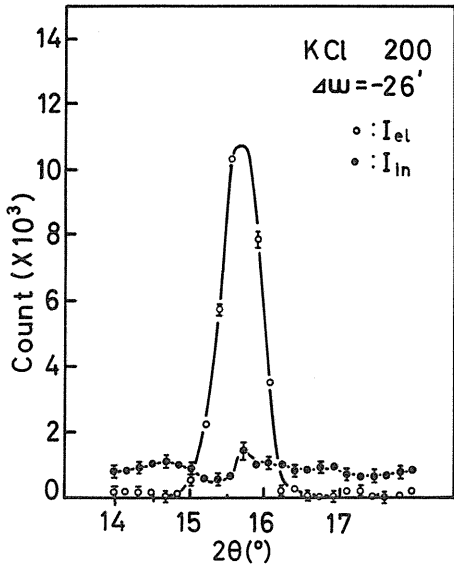1) By means of the Mössbauer γ-ray diffraction using the position sensitive detector, the elastic and inelastic intensity profiles in the Bragg reflections were measured separately with energy resolution about a few 10^{-8} eV and angular resolution of scattered beam about 10 minutes in the horizontal diffraction plane.

2) The dip of the inelastic intensity profile was found near every Bragg reflection measured.

3) If the glancing angle θ_0 of the incident beam deviates through $\Delta\omega$ from the Bragg angle θ_B, the direction corresponding to the minimum of the inelastic intensity dip deviates through $\Delta\omega$ from the direction of the intensity maximum of the Bragg reflection.

4) The main part in the inelastic intensity profile is estimated to be TDS.

We have the conclusion that the oberved dip of the inelastic intensity profile near Bragg reflection is caused by Bargg reflection of TDS. The dip corresponds to the defect line in the diffuse scattering observed in the diffraction pattern of X-ray film.

The dip of the inelastic intensity profile may be observed in TDS of other material under the following conditions. The crystal is mosaic enough to cause the kinematical diffraction or secondary extinction. Angular resolution of the detector is high enough to be able to detect the dip. Energy resolution of the detector system is high enough to separate elastic scattering and inelastic scattering such as TDS. The observation of the dip is easy for crystals from which TDS is very strong. The Mössbauer diffraction and the position sensitive detector play important roles to detect the dip. The conventional X-ray source and detector find difficulty in revealing the existence of the dip due to their poor angular and energy resolutions used so far. X-ray film is useful to find the two dimensional diffraction pattern of the defect line. However, inelastic scattering in the Bragg reflection cannot be separated from elastic scattering.

References

1) D. A. O'Connor and N. M. Butt: Phys. Lett. **7** (1963) 233.
2) G. Albanese, C. Ghezzi, A. Merlini and S. Pace: Phys. Rev. **B5** (1972) 1746.
3) V. S. Zasimov, N. N. Lobanov, J. Rudiger and R. N. Kusmin: Phys. Status Solidi (a) **38** (1976) K45.
4) M. Müllner, J. Maetz and H. Jex: Phys. Status Solidi (a) **56** (1979) 546.
5) Y. Kashiwase and M. Minoura: Jpn. J. Appl. Phys. **20** (1981) No.7, L.515.
6) Y. Kashiwase, Y. Kainuma and M. Minoura: J. Phys. Soc. Jpn. **51** (1982) 937.
7) Y. Kashiwase, Y. Kainuma and M. Minoura: Acta Cryst. **A38** (1982) 390.
8) Y. Oya and Y. Kashiwase:J. Phys. Soc. Jpn. **57** (1988) 2026.
9) Y. Kainuma: J. Phys. Soc. Jpn. **16** (1961) 228.
10) Y. Kashiwase, Y. Kainuma and M. Minoura: J. Phys. Soc. Jpn. **50** (1981) 2793.
11) Y. Kashiwase, Y. Kainuma and M. Minoura: Jpn. J. Appl. Phys. **21** (1982) L34.

IV. Preliminary Study on Nuclear Resonance Filtering

4.1. Introduction

It was pointed out first by Ruby[1] that the brightness of synchrotron radiation (SR) within the highly monochromatic region of a nuclear resonance width 10^{-8} eV exceeds that available from natural γ-ray source in the 10-keV X-ray region. Thus, using pure nuclear resonance scattering, one can produce an ultra narrow band pass filter to filter synchrotron radiation. Moreover, Mössbauer γ-rays from radioactive isotopes have such inherent problems as 1) existence of short life time, 2) low intensity and low emittance due to isotropic emission and self absorption, 3) large background of radiations due to precursor transitions accompanying emission of Mössbauer γ-rays.

After a number of authors[2,3] have investigated the problems of filtering, Cohen et al.[4] observed nuclear resonance curve using a gated detector developed to observe the conversion electrons produced from ^{57}Fe foil excited by SR. Chechin et al.[5] observed an enhancement of delayed counts behind an ^{57}Fe$_2$O$_3$ single crystal positioned for the 777 pure nuclear reflection. Gerdau et al.[6] have obtained the first definitive Mössbauer spectrum after the two ^{57}Fe-yttrium iron garnet single crystal films with a stainless steel absorber. Faigel et al.[7] first measured the full time evolution of the pure nuclear 777 reflection from ^{57}Fe-enriched hematite. Development of nuclear resonance filtering of synchrotron radiation recently has been achieved by some investigators[7,8,9].

Nuclear resonance filtering of synchrotron radiation produces revolutionary X-ray beams with characteristics 1) extremely narrow bandwidth (10^{-8} eV $\sim \mu$eV), 2) small angular divergence (mrad. $\sim \mu$rad.), 3) narrow time spectra (nsec $\sim \mu$sec), 4) quantum beat in time spectra, 5) high polarizability. These characteristics resulting from the coupling of the properties of synchrotron radiation with those of the collective nuclear resonance scattering cannot be obtained with the radioactive source and they surpass the radiation from the radioactive source. Thus, Mössbauer γ-rays from radioactive isotopes will be replaced by the filtered synchrotron radiation. Such a monochromatic source will offer a new field of study about inelastic-excitation with the small energy transformation. It has the potential of such applications as structure determination of biomolecule and magnetic material, studies of surface and thin film, interferometry, Mössbauer spectroscopy, etc.

As mentioned above, some methods already have been developed for nuclear resonance filtering. They are uses of (1) crystal monochromater, (2) such single crystal monochromator as ^{57}Fe$_2$O$_3$ which selects an electronically forbidden and nuclear allowed reflection, (3) time gated detector with high time-resolution and time spectroscopy, which separate spontaneous nonresonance radiations and delayed resonance radiation, (4) grazing-incidence antireflection (GIAR) film and mutilayer thin film mirrors to suppress nonresonance radiation and generate resonance radiation by exciting Mössbauer isotopes contained, (5) polarizer and analyzer to suppress nonresonance radiation. The methods (1)−(3) have been well developed and useful already. However, the fourth and the fifth are still far from practical use.

This chapter reviews present authors' preliminary study[10−14] of the above (1), (4) and (5) methods for nuclear resonance filtering of synchrotron radiation performed at the PF, BL-14B of the KEK in Tsukuba.

4.2. Suppression of Harmonics of 14.4 keV Synchrotron Radiation[12,13]

For monochromatization of synchrotron radiation to bandwidth 10^{-8} eV by nuclear resonance filtering, suppression of enormous background scattering due to electron is the most important problem in the study.

The purpose of this study is to make contamination of harmonics of 14.4 keV clear and to suppress the harmonics using different refraction effects in asymmetric 10 64 reflection and symmetric 10 64 consecutive reflection from grooved surfaces of a silicon single crystal. Principle of this method were proposed first by Bonse et al.[15], and developed by some investigators[16,17].

Energy spectra of the synchrotron radiations monochromatized by the Si 111 double symmetric reflections and the double 10 64 reflections from a grooved Si single crystal were observed at the PF, BL-14B using a pure germanium solid state detector and a multichannel analyzer as shown in Fig. 1. Synchrotron positron energy and current were 2.5 GeV and about 300 mA, respectively. The radiation flux was lowered enough to protect the detector using a slit system. The counting rate of 14.4 keV photon was about 1000 cps.

Figure 2(a) and (b) show energy spectra of the beam monochromatized by the double symmetric 111 reflection and plus the double symmetric 10 64 reflections, respectively. We can find the third, the fourth and the fifth intense harmonics of 14.4 keV radiation. The second harmonics is suppressed by the 222 forbidden reflection of silicon pre-monochromator. Sharp peaks of 3.4 keV and 3.5 keV are escape peaks from detector germanium.

Figure 2(c) shows an energy spectrum of the beam monochromatized by the asymmetric 10 64 reflection and the symmetric 1064 consecutive reflection. A satisfactory suppression of the harmonics can be seen from the figure. Energy resolution about 10 meV was obtained using (+,+) arrangement of the Si (10 64) channel-cut crystal monochromators.

S1,S2   Slit
BFM   Beam Flux Monitor   C1 grooved Si crystal with
SSD   Solid State Detector   the (10 64) reflection plane
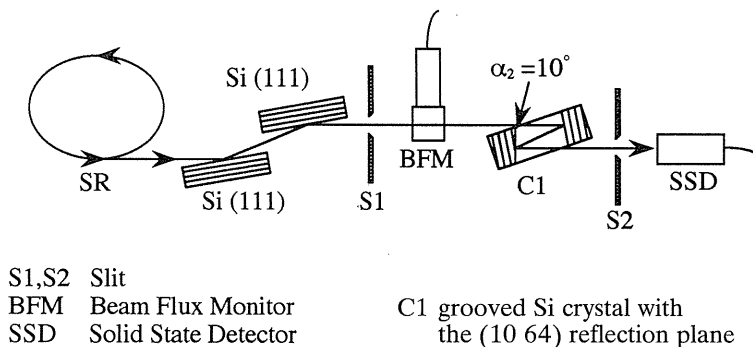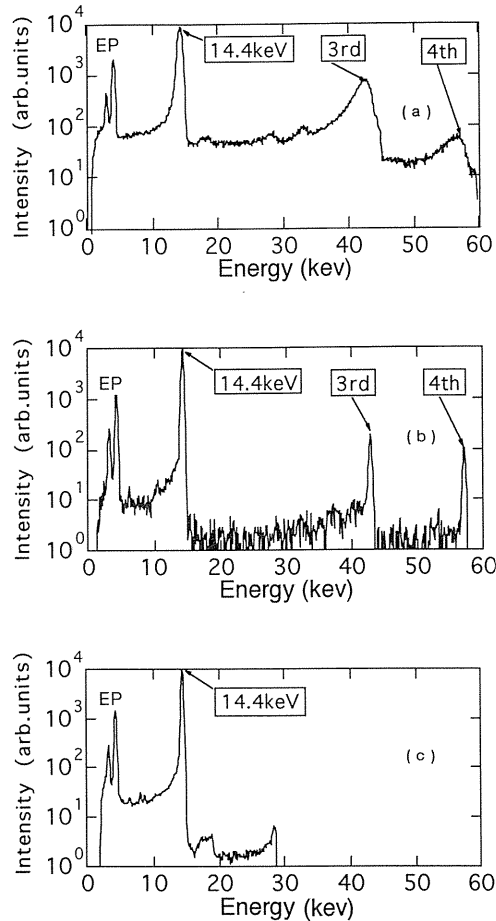
Fig. 1. Instrumental arrangement.

Fig. 2. (a) Observed spectrum of double symmetric 111 reflections, (b) Observed spectrum of double symmetric 10 64 reflections, (c) Observed spectrum of asymmetric and symmetric 10 64 consecutive reflections.

4.3. GIAR-Film Mirror[10,11]

For the purpose of producing filters to monochromatize synchrotron radiation to bandwidth of $10^{-6} - 10^{-8}$ eV by nuclear resonance scattering, an interference technique for X-ray optics, grazing-incidence antireflection (GIAR) film, was proposed[18] and then, theoretical[19] and experimental investigations[20-22] were developed. The film is designed to suppress enormous electronic background reflection in the angular region where nuclear-resonance reflection amplitude is large near the critical angle of total reflection. The advantages of the GIAR-films are (1) crystals which have restrictions imposed by Bragg reflection and crystal structure are unnecessary due to total reflection, zeroth-order reflection. The films require only flat surface and flat interface between layers of uniform material, (2) the films are relatively easy

to produce by applying improved technique of thin-film fabrication, (3) the film-mirror is relatively freed of heating or radiation damage, and then stable against lattice-parameter change, (4) the films can be designed to produce filter of very broad resonance width $\Delta \omega = 100\Gamma$, where Γ is a natural width, or narrow resonance width $\Delta \omega = \Gamma$. However, the films have such negative side as the filter can not accept full beam flux of the incident synchrotron radiation, because of small effective cross-section of the incident beam limited by the size of the mirror and the small angle grazing-incidence geometry. Although, this problem will be overcome soon using high emittance of the synchrotrn radiation produced by a dedicated undulator. The GIAR- films, however, are still far from practical use.

The purpose of this study is to prepare and test the GIAR films by an experiment of X-ray interference between reflections from the film.

Iron enriched with 90% ^{57}Fe was evaporated in the vacuum of about 10^{-6} Torr. An about 250Å thick ^{57}Fe film coated with about 90Å thick Al film was deposited on a 30 × 100 mm^2 flat surface of a quartz glass plate with thickness 10 mm. The ^{57}Fe layer in the specimen GIAR-film was examined by Mössbauer spectroscopy in which X-rays emitted in back direction accompanying emission of conversion electrons from the film irradiated by radiations from 25 mCi ^{57}Co in rhodium matrix were measured with a scintillation counter using Mössbauer spectroscopy instruments. Figs. 3(a) and (b) show Mössbauer spectra of resonant X-rays from ^{57}Fe contained in a natural ion foil and from the ^{57}Fe layer of the specimen GIAR film, respectively. The figures show that the ^{57}Fe layer of the specimen film has bcc, α-iron, structure. The reflectivity curve of the specimen was measured by means of the
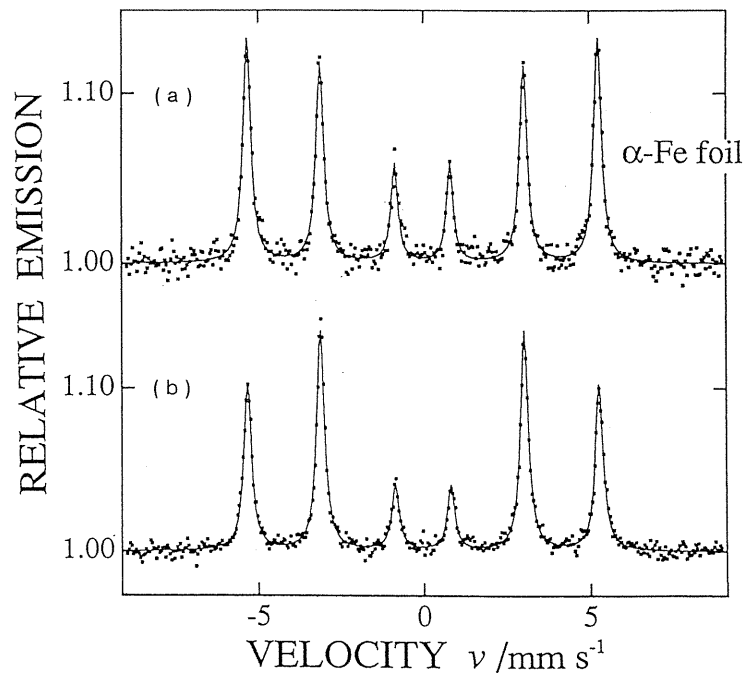

Fig. 3. (a) Mössbauer spectrum of natural ion foil. (b) Mössbauer spectrum of the specimen GIAR film.

GIAR film, respectively. The figures show that the ^{57}Fe layer of the specimen film has bcc, α-iron, structure. The reflectivity curve of the specimen was measured by means of the optical system installed on the BL-14B shown in Fig. 4 and 0.8602Å radiation monochromatized finally by the 1064 double reflections from a channel-cut Si crystal. The angular divergence of the incident beam is about 1″.

Figure 5 shows the reflectivity curve of the specimen. Open circles show the experimental result and solid curve show the theoretical calculation made by using model parameters shown in Table 1. Each row in Table 1 indicates parameters of three layers from the top surface of elements in the second column. The fitting parameters are electron densities N, thickness l of the layers and standard deviations σ indicating surface roughnesses and boundary roughnesses between the layers obtained on the basis of the Nevot-Croce method[23]. The parameters δ and β are the real and imaginary parts of deviation from unity of refractive index.
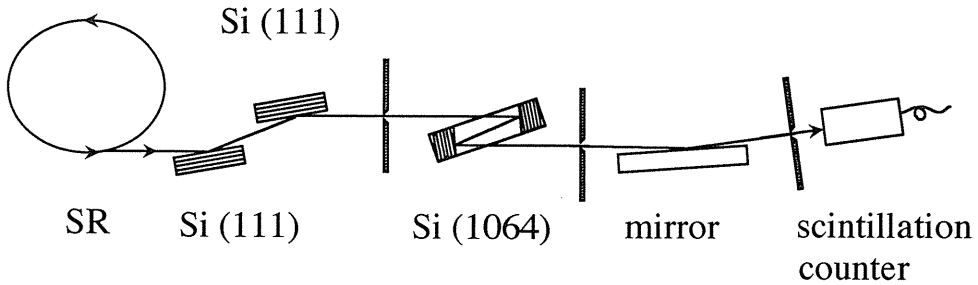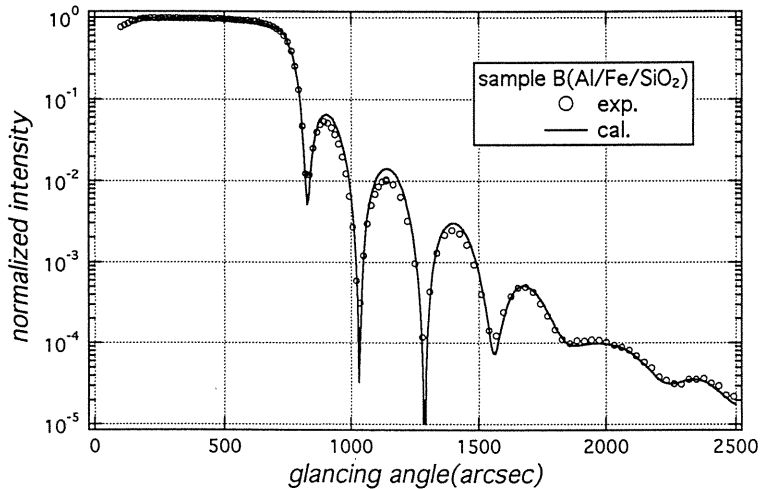

Fig. 4. Instrumental arrangement.

Fig. 5. Reflectivity curve.

Table 1. Model parameters of electron density N, real part δ of deviation from unity and imaginary part β of refractive index, thickness ℓ of layers and interface roughness σ of the film.

	element	$N\,(\text{Å}^{-3})$	$\delta\,(\times 10^{-6})$	$\beta\,(\times 10^{-7})$	$\ell\,(\text{Å})$	$\sigma\,(\text{Å})$
layer 1	Al	0.64	2.1	1.2	70	16
layer 2	Fe	1.99	6.6	2.8	245	17
layer 3	Fe	1.47	4.9	2.1	14	12
substrate	SiO_2	0.69	2.3	0.097	∞	6

Table 2. Peak resonant reflectivities $|R_r|^2$, effective width Γ_{eff} in the unit of natural width 4.7×10^{-9} eV, and signal-to-noise ratio $|R_r|/|R_{nr}|^2$ for the ideal sample in Table 1, where enrichment of ^{57}Fe is 100% at ϕ_0 in the case of no Zeeman splitting: the $1/2 \to 3/2$ transition reflection, $\mathbf{e}_{+1}$ radiation with $\boldsymbol{B} /\!/ \boldsymbol{k}_0$, and recoiless fraction $\exp(-k^2 <x^2>) = 0.7$.

	ϕ_0	Γ_{eff}	$|R|^2_r/|R|^2_{nr}$	$\Gamma_{\mathrm{eff}}/20\,\text{meV}$	$(|R|^2_r)^2\Gamma_{\mathrm{eff}}/20\,\text{meV}$
sample A	820″	124Γ	45 (0.90/0.02)	2.9×10^{-5}	2.3×10^{-5}
	1000″	23Γ	$1.7 \times 10^3\ (0.85/5 \times 10^{-4})$	5.4×10^{-6}	1.7×10^{-6}
sample B	830″	90Γ	91 (0.91/0.01)	2.1×10^{-5}	1.7×10^{-5}
	1030″	20Γ	$2.2 \times 10^3\ (0.85/3 \times 10^{-4})$	4.7×10^{-6}	3.4×10^{-6}

The Table 2 shows the effective energy width Γ_{eff} of nuclear resonance reflection, reflectivity ratio $|R_r|/|R_{nr}|^2$ between resonance and nonresonance reflections at glancing angle ϕ_0 for the film model of Table 1, in which ^{57}Fe enrichment is 100%. The angle ϕ_0 in the Table 2 describes the position of the first and the second minima in Fig. 5. The values of Γ_{eff} and $|R_r|^2$ are calculated from the formulas given by Hannon et al.[19] From the value in the last column, we can estimate observation feasibility of a few resonant photons per second., if we can use 10^6 cps incident photons with energy 14.41 keV in the energy range $\Delta E = 20$ meV for double reflections of film mirrors in the Table 1. Good simulation of the curve fitted to an observed interference pattern is obtained by assuming a three-layer model with boundary roughnesses 10—20Å between the layers.

4.4. Suppression of Nonresonance Radiations by Polarizer[14]

Electronic scattering vanishes for a 90° scattering in the direction of the incident linear σ-polarization, while there will generally be nuclear resonance scattering. When scattered beams are mixed with σ-polarized electronic scattering and π-polarized nuclear resonance

scattering, which can be generated from a GIAR-film of enriched ^{57}Fe irradiated by σ-polarized incident beam, the resonance scattering can be separated[24] by suppressing σ-polarized electronic scattering with an analyzer at a scattering angle $2\theta_B = 90°$.

The aim of this study is to develop the polarizer and the analyzer for producing pure σ- or π-polarized beams, and then, to suppress nonresonant scattering and detect separately the nuclear resonance scattering. The principle of this method has been proposed by some investigators[25,26].

Polarizers of $2\theta_B = 90.2°$ for 14.4 keV radiation were produced using the asymmetric and symmetric 840 reflections from grooved surfaces of a silicon single crystal. The angular width of the 840 reflection measured with a Si (840) analyzer in the $(+, +)$ geometry is about $1''$, which is close to the theoretical width $0.36''$. The σ- and π-polarized components of the radiations monochromatized and polarized by the double 840 reflections are observed with the Si (840) analyzer and a scintillation counter at BL-14B as shown in Fig. 6(a) and (b).

(a)
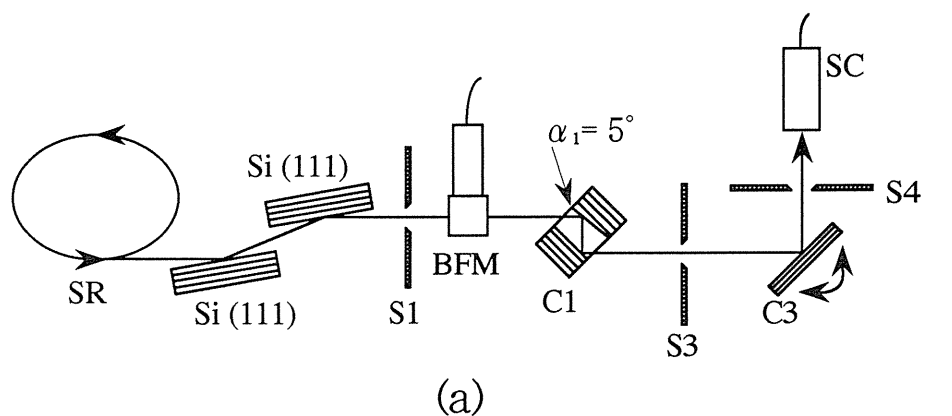
S1-S4   Slit
BFM   Beam Flux Monitor
SC   Na(I) Scintillation Counter
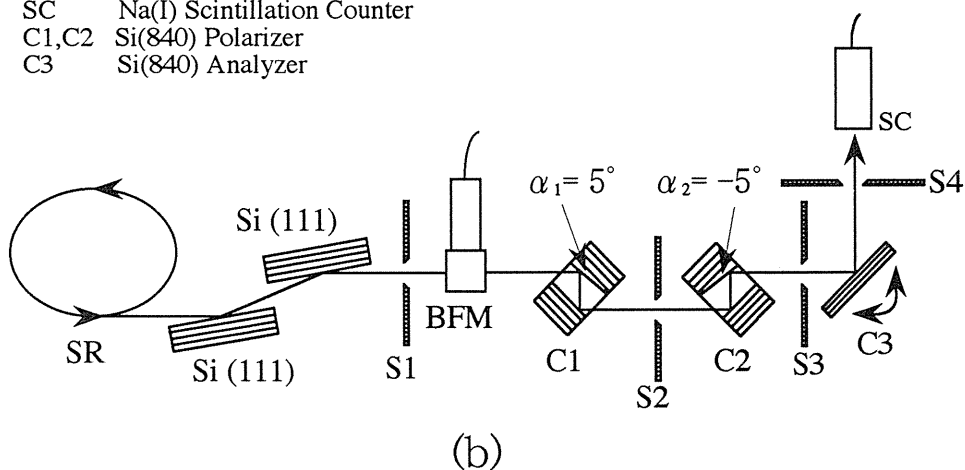C1,C2   Si(840) Polarizer
C3   Si(840) Analyzer
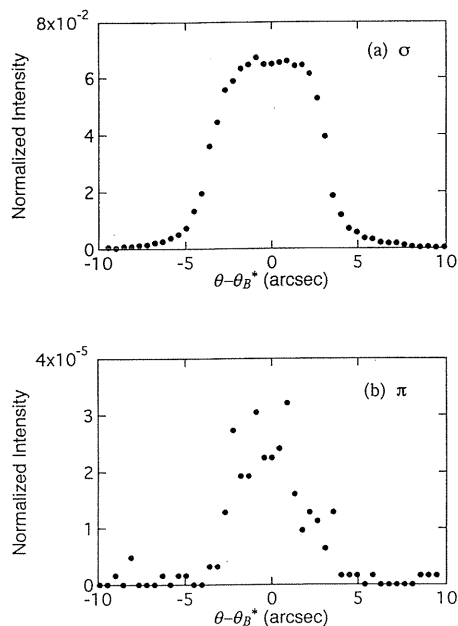
(b)

Fig. 6. Instrumental arrangement.

Fig. 7. Rocking curves observed by step scan-
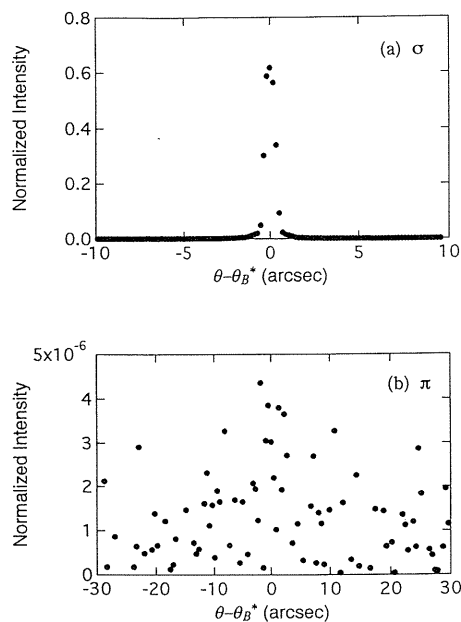ning analyzer C3 in Fig. 6(a).

Fig. 8. Rocking curves observed by step scan-
ning analyzer C3 in Fig. 6(b).

Energy and current of synchrotron beam were 2.5 GeV and about 300 mA, respectively. The analyzer crystal was set on a four-circle goniometer. The rocking curves of the σ-, π-components were measured by step-scanning around the horizontal and vertical axes.

Figures 7(a) and (b) show rocking curves of the σ- and π-components, respectively, which are measured with C1 monochromator as shown in Fig. 6(a) and normalized with the intensity of the beam incident on the analyzer. Counting rates at the peak of the σ- and π-components are 4.2×10^4 cps and 20 cps, respectively. The integrated intensity ratio I_π/I_σ is 2.9×10^{-4}, which is much larger than calculated value 1.8×10^{-6}. The disagreement between the calculation and the experimental result is due to large angular divergence of the incident beam in the plane parallel to the direction of the σ-polarization vector. Figs. 8(a) and (b) show curves of the σ- and π-components, which are measured with C1 and C2 monochromators as shown in Fig. 6(b). Energy resolution about 25 meV was obtained using $(+,+)$ arrangement of the Si (840) channel-cut monochromators.

4.5. Summary, Conclusion and Discussion

Three methods to suppress electronic scattering investigated for nuclear resonance filtering of 14.4 keV synchrotron radiation made clear the followings. Satisfactory suppression of higher harmonics is obtained using the symmetric and asymmetric 10 64 reflections in a channel-cut Si monochromator. Suppression possibility of electronic scattering up to 10^{-6} is

obtained using GIAR-film double reflections or combination of GIAR-film mirror with the 840 polarizer and analyzer, simultaneously. The authors can obtain energy resolution about 10 meV using $(+, +)$ arrangement of channel cut Si (10 64), or (840) monochromators. Production of a few cps resonant photons is estimated to be possible, if 10^6 cps photons of 14.4 keV in the energy region $\Delta E = 20$ meV is incident effectively on GIAR film mirror. The maximum photon flux 1×10^4 cps was obtained (1×10^6 cps has not been) by the present authors' experiment at PF, BL-14B. Production of a few cps resonant photons using our GIAR film mirror may be possible at AR, NE3, where brilliance and photon flux are 10^2 times higher than at BL-14B.

Recently, present authors could observe 15 cps of 14.4 keV nuclear resonance photons near the critical angle for total reflection of X-rays by electron using monochromatized 14.4 keV synchrotron radiation in a nsec short-time pulse mode incident on the sample B at AR-NE3 of the KEK[27]. The delayed nuclear resonance scattering as well as prompt components were measured separately. The development of brilliant synchrotron source with low emittance is necesary for nuclear resonance filtering with GIAR-film. Dedicated undulator beam line at SPring 8 under construction may be useful for this purpose.

References

1) L. Ruby: J. Phys. Colloq. **35**, C6 (1974) 209.
2) A. M. Afanas'ev and Yu Kagan: Sov. Phys.-JETP **21** (1965) 215, **27** (1968) 819, J. Phys. **C12** (1979) 615.
3) J. P. Hannon and G. T. Trammell: Phys. Rev. **169** (1968) 315, **186** (1969) 306, **B9** (1974) 2791.
4) R. L. Cohen, G. L. Miller and K. W. West: Phys. Rev. Lett. **41** (1978) 381.
5) A. J. Chechin, N. V. Andronova, M. V. Zelepukin, A. N. Artemev and E. P. Stepanov: JETP Lett. **37** (1983) 633.
6) E. Gerdau, R. Rüffer, H. Winkler, W. Tolksdorf, C. P. Klages and J. P. Hannon: Phys. Rev. Lett. **54** (1985) 835.
7) G. Faigel, D. P. Siddon, J. B. Hastings, J. R. Grover, J. P. Remaika and A. S. Cooper: Phys. Rev. Lett. **58** (1987) 2699.
8) U. van Bürck, R. L. Mössbauer, E. G. Gerdau, R. Rüffer, R. Hollatz, G. V. Smirnov and J. P. Hannon: Phys. Rev. Lett. **58** (1987) 355.
9) S. Kikuta, Y. Yoda, Y. Hasegawa, K. Izumi, T. Ishikawa, X. W. Zhang, S. Kishimoto, H. Sugiyama, T. Matsushita, M. Ando, C. K. Suzuki, M. Seto, H. Ohno and H. Takei: Hyperfine Interactions **71** (1992) 1491.
10) JAERI-RIKEN SPring 8 Projict, 1990−1991. Subgroup of Nuclear Bragg Scattering and Condensed Matter Experiments.
11) Y. Kashiwase, K. Kaneko, I. Nishida, M. Kogiso, M. Mori, M. Minoura, Xiao Wei Zhang and T. Kado: Photon Factory Activity Report P.334 (1992).
12) A. Kitabatake, Y. Kashiwase, M. Kogiso, M. Mori, M. Minoura, K. Hirano and X. W. Zhang KEK PF Activity Report, P.318 (1993).
13) K. Kaneko: Master thesis, Nagoya Univ. School of Engin., Dept. of Appl. Phys., 1993.
14) A. Kitabatake: Master thesis, Nagoya Univ. School of Engin., Dept. of Appl. Phys., 1995.
15) U. Bonse, G. Materlik and W. Schröder: J. Appl. Cryst. **9** (1976) 223.
16) M. Hart and A. D. Rodrigues: J. Appl. Cryst. **11** (1978) 248.
17) T. Matusita and H. Hashizume: Handbook on Synchrotron Radiation Vol.1, edited by E. E. Koch, 251−304 (1983) Amsterdam, North-Holland.
18) J. P. Hannon, G. T. Trammel, M. Mueller, E. Gerdau, H. Winkler and F. Rüffer: Phys. Rev. Lett., **43** (1979) 636.

19) J. P. Hannon, H. V. Hung, G. T. Trammel, E. Gerdau, M. Mueller, R. Rüffer and H. Winkler: Phys. Rev., **B32** (1985) 5068, 5081, 6363.
20) M. Grote, R. Röhlsberger, M. Dimer, E. Gerdau, et al.: Europhys. Lett., **17** (7) (1991) 707.
21) W. Sturhahn, E. Gerdau, R. Hollaz, R. Rüffer, H. D. Rüter and W.Tolksdorf: Europhys. Lett. **14** (1991) 821.
22) E. E. Alp, T. M. Mooney, T. Toellner, W. Sturhahn, E. Witthoff, R. Rölsberger, E. Gerdau, H. Homma and M. Kentjana: Phys. Rev. **70** (1993) 3351.
23) L. Nevot and P. Croce: Rev. Phys. Appl. **15** (1980) 761.
24) D. P. Siddons, J. B. Hastings, G. Faigel, L. E. Bergman, P. E. Haustein, and J. R. Grover: Phys. Rev. **62** (1989) 1384.
25) Y. Kashiwase: The 3rd Annual Meeting of Japan Society of Synchrotron Radiation, Osaka, April 1990.
26) D. P. Siddons, U. Bergmann and J. B. Hastings: Phys. Rev. Lett. **70** (1993) 359.
27) M. Kogiso, Y. Ito, T. Shimogawa, Y. Kashiwase, Y. Kobayashi, S. Hiyama, S. Nasu, X.W. Zhang and K. Hirano: The 51st Annual Meeting of the Physical Society of Japan, Kanazawa, April 1st, 1996.

Acknowledgment